Electromagnetic Methods For Thermal Therapy Monitoring and Assessment

Keith D. Paulsen, Alex Hartov, Paul M. Meaney
Thayer School of Engineering, Dartmouth College, Hanover, NH 03755

ABSTRACT

The desire for noninvasive monitoring of thermal therapy is readily apparent given its intent to be a minimally-invasive form of treatment. Electromagnetic properties of tissue vary with temperature; hence, the opportunity exists to exploit these variations as a means of following thermally-based therapeutic interventions. The review describes progress in electrical impedance tomography and active microwave imaging towards the realization of noninvasive temperature estimation. Examples are drawn from the author's experiences with these technologies in order to illustrate the principles and practices associated with electromagnetic imaging in the therapy monitoring context.

Keywords: Electrical impedance tomography, impedance spectroscopy, microwave imaging, thermal imaging, bioelectromagnetics

1. INTRODUCTION

Electromagnetic methods have been used extensively to deliver thermal therapy as described throughout this review volume. Developments have included a variety of source configurations and frequency bands with therapeutic goals ranging from the induction of mild hyperthermia (elevations a few degrees above core body temperature) to the thermal ablation of the target zone (elevations above the temperature of blood coagulation). Far less developed is the idea of using electromagnetic methods to monitor and assess thermal therapy through noninvasive sensing. The genesis for considering whether electromagnetic technology can serve in this role is the observation that the electromagnetic properties of most tissues are temperature dependent[1-3]. Hence, if one could devise a scheme for imaging electromagnetic property changes noninvasively, it might be possible to track the evolution of temperature rise in tissue during the course of thermal therapy. This chapter will review efforts to use electromagnetic methods for therapy monitoring and assessment.

Specifically, active technologies will be investigated. For the purposes of this chapter active will imply that the electromagnetic methods under review deploy a probing signal over particular bands of the frequency spectrum in order to excite a tissue response which is used to infer the spatial distribution of the electrical properties within the tissue volume of interest. This is in contrast to passive strategies which infer temperature data based on the natural electromagnetic emissions that emanate from thermally stimulated tissue. These radiometric methods, typically applied over the microwave[4-6] and infrared[7-8] spectrums, have been used successfully in a variety of settings including some which are related to thermal therapy[9-11]. However, radiometric methods are often confined to the first few centimeters of tissue and largely amount to one-dimensional depth profiling because of their poor lateral resolution which is limited by the aperture size of the sensing radiometer — often many centimeters in scale.

Active technologies offer the possibility of multi-dimensional imaging at finer spatial scales, although it remains to be seen whether they can monitor temperature

Matching the Energy Source to the Clinical Need: A Critical Review, edited by Thomas P. Ryan,
Proceedings of SPIE Vol. 10297, 102970J · © 2017 SPIE
CCC code: 0277-786X/17/$18 · doi: 10.1117/12.375220

changes at spatial resolutions below one centimeter and thermal resolutions of less than one degree centigrade. This review will focus on electrical impedance imaging, usually identified by the use of electric currents oscillating below 10 MHz, and microwave imaging, encompassing the use of electromagnetic signals at frequencies below 3 GHz and as low as 300 MHz. In each case, the basic physical principles involved with the method will be described followed by a historical review of the major accomplishments which have been achieved to date. Emphasis will be directed towards those results of particular importance to thermal therapy monitoring and assessment, although some attention will be given to other related applications of these methods. For each method, representative examples of state-of-the-art findings will be presented and discussed. In this regard, data will be drawn largely from the author's experiences with these technologies. The intent is to illustrate current progress rather than provide an exhaustive review of the complete spectrum of results that are available in the literature. The hope is that this will provide the reader with a sense of how far electromagnetic methods have progressed towards the goal of monitoring and assessing thermal therapies.

2. ELECTRICAL IMPEDANCE IMAGING

2.1 Physical Principles

Electrical Impedance Imaging or Electrical Impedance Tomography (EIT) exploits low frequency electrical signals in the 10 KHz to 10 MHz range to determine tissue electrical properties over this portion of the electromagnetic spectrum. At these frequencies, electric fields induced in the body are created through direct contact electrodes. Two modes of operation are possible. Current mode drives known current patterns through surface electrodes positioned around the body in the region of interest. These injected currents cause an electric potential distribution to develop at measuring electrodes which depends on the electrical property constituents within the tissue. Images are formed by estimating the electrical property profile needed to create the measured potential distribution given the known driving current patterns. Voltage mode is the other operational approach. In this case the role of voltage and current are exactly reversed (compared to current mode). A predetermined voltage pattern is applied to the surface electrodes and the resulting current distribution is measured. The electrical properties of the intervening tissue dictates how the induced currents will flow. Figure 1 contains a conceptual drawing of the EIT process. It illustrates how contact electrodes are placed around the tissue in order to produce an image of the region of interest.

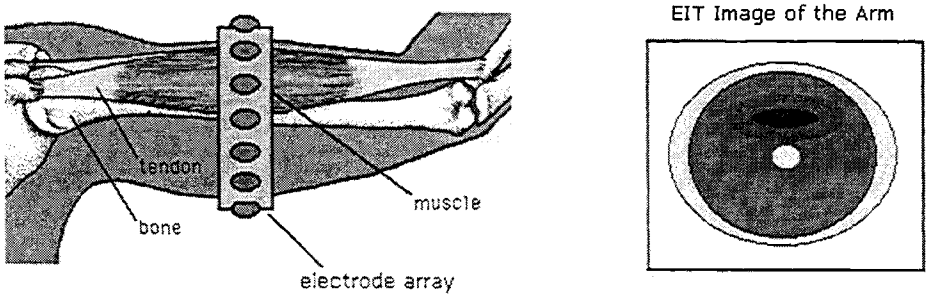

Figure 1: Schematic of the electrical impedance imaging process.

A recent set of articles by Gabriel et. al. summarizes much of the existing knowledge on the electrical properties of many normal tissues over a wide frequency band[12-14]. These properties are characterized by their electrical conductivity, σ, and

electrical permittivity, ε, which can exhibit considerable dispersion over the frequencies of interest. Alterations in tissue impedance spectra are known to occur with changes in physiological state and considerable effort has been directed towards the exploitation of these spectral signatures for the diagnosis and characterization of tissue pathology and/or pathophysiology. For example, electrical properties (in particular electrical conductivity) are known to vary by approximately 2%/°C in most tissue[1-3].

In the frequency range relevant to EIT, tissue electrical impedance is sensitive to cellular morphology and tissue microarchitecture. Particularly important are membrane structures, both intra- and extracellular, which are critical sites associated with thermally induced tissue damage. At the low frequency end of the spectrum, the outer cell membrane is able to charge completely within the time required to complete one period of the applied oscillating electromagnetic field. A constant voltage is then established at the membrane surface over most of each cycle. The oscillating current that flows inside the cell due to membrane voltage changes is negligible for a large fraction of each period, limiting the electrical current flow to the extracellular medium. As the frequency of the applied field is increased, a point is reached where the time required to charge the intra and extracellular membrane is long relative to the duration of the period, creating a persistent voltage change at these membranes which translates into a sizable intracellular current flow. At even higher frequencies, dipolar reorientation of proteins and tissue organelles can occur. Hence, the electrical property spectrum for higher frequencies contains information about the intracellular environment making it well-suited for sensing tissue changes due to a thermal insult.

At frequencies below 10 MHz, electromagnetic fields in tissue are governed by the complex-valued Laplace equation

$$\nabla \cdot (\sigma - i\omega\varepsilon)\nabla\Phi = 0 \tag{1}$$

where σ is the electrical conductivity, ε is the electrical permittivity, ω is the angular frequency of the applied currents (current mode) or impressed voltages (voltage mode), i is the square root of -1, and Φ is the resulting electrical potential. In current mode, the potential distribution is driven by an enforced current density distribution on the body surface at the electrode sites such that

$$(\sigma - i\omega\varepsilon)\hat{n} \cdot \nabla\Phi = -J_{in}\,\hat{n} \tag{2}$$

on the electrode and zero elsewhere, $\hat{n}$ is the outward-pointing normal direction on the electrode surface and J_{in} is the applied current density. Voltage mode is mathematically similar except that Φ is dictated at the electrodes and J in (2) is the measured quantity.

The majority of efforts to recover spatial distributions of electrical properties, σ and ε, from the impedance data have exploited advanced computational methods. Generally, two strategies have emerged. The first is back-projection which is common in CT; however, rather than back-project along straight lines (as with x-rays), curved paths are used which are derived from solutions to (1) when a localized current (or voltage) stimulus is applied at one point (electrode) on the boundary and measured at other points (electrodes) on the tissue surface[15-18]. Back projection algorithms are fast providing the opportunity for real-time imaging of physiological process such as lung air volume[19-20]; however, they have generally not been quantitative with respect to the electrical properties that are recovered. They provide useful visual images of electrical property contrast but they do not accurately estimate the actual property values.

The second approach is model-based methods which repeatedly solve (1) to estimate electrical property distributions[21-24]. These schemes are essentially optimization problems which seek to find the electrical property profiles which allow the model (i.e. equation 1) to best match the data according to some criterion. Typically, least squares objectives are used to find the best data-model match, although multi-component

objectives which include additional criteria such as total variation minimization have also been considered. These algorithms have often deployed a numerical method such as finite elements to compute solutions to (1); however, in certain cases analytical methods have proved successful as well. Minimization of the squared error objective function leads to a nonlinear system of equations that can be solved with classical techniques such as Newton's method. Property estimation based on iteratively minimizing the squared error between computed and measured data (voltage in current mode or current in voltage mode) requires computation of the rate of change of the solution to (1) for a small change in tissue electrical properties at a single location in the tissue volume of interest. While numerical differentiation is one approach which has been used, it is also possible to develop a partial differential equation in terms of the desired derivatives. In particular, differentiating equation (1) with respect to the kth member of an expansion function that defines the electrical conductivity distribution as

$$\sigma = \sum_{k=1}^{N} \sigma_k \varphi_k$$

leads to

$$\frac{\partial}{\partial \sigma_k}\left[\nabla \cdot (\sigma - i\omega\varepsilon)\nabla\Phi\right] = \nabla \cdot \frac{\partial \sigma}{\partial \sigma_k}\nabla\Phi + \nabla \cdot (\sigma - i\omega\varepsilon)\nabla\left(\frac{\partial \Phi}{\partial \sigma_k}\right) = 0 \quad (3)$$

Defining $\frac{\partial \Phi}{\partial \sigma_k} = \Phi'$, equation (3) becomes

$$\nabla \cdot (\sigma - i\omega\varepsilon)\nabla\Phi' = -\nabla \cdot \frac{\partial \sigma}{\partial \sigma_k}\nabla\Phi \quad (4)$$

which is identical to equation (1) in the quantity Φ' except for the occurrence of the right-hand-side quantity expressed in terms of Φ. Once equation (1) is solved for Φ for the current estimate of the electrical properties, σ and ε, equation (4) can be computed for the derivative of the solution with respect to all of the σ_k values which parameterize the electrical conductivity distribution throughout the tissue region of interest. A similar equation can be developed for derivatives with respect to the permittivity profile. These derivatives define the Jacobian or sensitivity matrix which is incorporated into the process of updating the electrical properties from an initial estimate. Because the measured surface quantities are nonlinear functions of the electrical property distribution, retaining the nonlinearity is essential if obtaining quantitative estimates of property values are desired.

Since image reconstruction in the model-based context is essentially a nonlinear optimization problem, a variety of solution schemes, beyond Newton's method exist to minimize the stated objective by evolving the tissue electrical property distribution. Included in the suite of possibilities are randomization processes which have also been investigated. For large parameterizations of the electrical properties, these random methods tend to become very slow, although they can be particularly useful for avoiding local minima in the solution space. Overall, however, Newton's method has been very popular having proved to be a reasonable compromise between computational costs and image quality for model-based image reconstruction for EIT.

3. Historical Perspective

Considerable progress was realized in the development of EIT as a general imaging method during the early to mid 1980s. The efforts of two groups — the

Sheffield team lead by Barber and Brown and the Renselaer team lead by Newell and Isaacson — were paramount in this regard. Under the direction of Brown several theoretical studies were conducted which helped to define characteristics of the imaging method, for example, its spatial resolution and depth sensitivity as a function of electrode number[25]. These were followed by investigations which led to the realization of a multi-channel hardware system championed by Barber[26-28]. Further developments resulted in image reconstruction based on back projection along curved paths defined by equipotential solutions to Laplace's equation[29-33].

The Sheffield group also pioneered the use of multiple frequencies to elicit the spectral responses of imaged tissue[34-36]. This spectroscopic electrical impedance tomography (EITS) technique, often referred to as electrical impedance spectroscopy (EIS) was first realized through a dual-frequency system which was later expanded to include the choice of up to eight discrete frequencies. Image reconstructions in laboratory phantoms and in the lung in vivo were demonstrated over the frequency band of the data collection. Image pixel spectral responses were also extracted showing for the first time true spatially-resolved EIS[34].

The RPI team contributed significantly towards the early development of EIT[37-40] as an imaging modality on both theoretical and practical grounds. In a landmark paper[41] Isaacson showed that the maximum distinguishability of an internal electrical heterogeneity occurred when currents were applied simultaneously to all peripherally-located electrodes in sinusoidal patterns of increasing spatial frequency. This finding lead to an intensive effort to realize high quality current drivers which could modulate the output amplitude at each electrode. Reconstruction algorithms based on analytical Laplace equation solutions that were used to update a homogeneous estimate of the electrical properties in a single iteration were shown to yield high quality electrical impedance images of objects placed in a saline tank[42-44]. Efforts to define and adaptively produce optimal current patterns using on-line measurements soon followed[45]. Images of both conductivity and permittivity distributions were demonstrated. Several advances to the RPI hardware system were reported over the years with the latest essentially providing real-time imaging through ultrafast parallel data acquisition and concomitant image reconstruction. In an impressive experiment, the RPI team showed the ability to reconstruct a high-contrast copper ball as it swung on a pendulum through a saline tank 30 cm in diameter[39]. While the exact size of the ball was not accurately resolved (it was blurred to a size of approximately 5cm), the data collection and image reconstruction was sufficiently fast and accurate enough to track the ball location.

The ideas for using EIT as a thermal imaging technique during therapeutic tissue heating first began to appear in the mid to late 1980s. Conway, Griffiths and Hawley reported important early experiences in this regard[46-49]. Images were two-dimensional involving idealized phantom studies which suggested that temperature resolutions on the order of a degree were possible to achieve. By the early 1990s efforts to integrate EIT systems with hyperthermia equipment were underway. Hawley and coworkers[48] combined EIT measurements in phantoms heated with a capacitive hyperthermia device operating at 27 MHz. The study included use of a heterogeneous phantom consisting of a 127 mm diameter muscle equivalent cylinder having foam inserts. Regional analysis around each of eight temperature probe locations showed that the EIT images yielded a good correlation with temperature increase over a 20 minute period with a standard error estimate of 0.75°C. However, in the central location of the phantom, EIT sensitivity to temperature changes was significantly compromised.

In vivo experiments were also conducted on volunteers who consumed liquids of temperatures of 37°C and 47°C. The order in which the liquids were introduced was randomized and an imaging experiment was performed at least twice at each temperature. Images were reported which showed changes in resistivity relative to an empty stomach.

The spatial resolution of the images produced was estimated to be 4-8 cm with a slice thickness ranging from 4 cm at the periphery to nearly 8 cm at the center; however, the temperature sensitivity could not be calculated from these qualitative experiments.

The group at Dartmouth expanded on these thermal experiments in phantoms[24,50] as well as in vivo in both animal[51] and human subjects[51,52]. These researchers developed the idea of exploiting internal measurements of electrical potential to improve the spatial resolution at depth with the EIT technique. In a series of simulation experiments involving a realistic body cross-section derived from anatomical CT scans of the pelvis, they showed mean and maximum temperature errors along catheter tracks as a function of the use of internal data and the degree of prior anatomical information that was available. Mean errors were less than 0.5°C with maximum errors generally less than 2°C that approached 1°C when internal data and prior information were used. In a follow-up series of simulations Paulsen and Jiang[53] found average temperatures were below 1°C provided prior anatomical information was included even in the face of added measurement noise of 1% and greater.

In a related set of phantom experiments, Moskowitz et. al.[50] found temperature predictions were accurate to better than 1°C on average when using data from surface electrodes combined with internal linear arrays. These experiments involved ultrasound heating of an agar target region suspended in gel confined within an 18 cm cylindrical tank. Sixteen stainless steel 3 cm electrodes were mounted to the inside boundary of the phantom container. The impedance hardware system operated in current mode applying the simultaneous excitation patterns of Isaacson which possess increasing spatial frequencies. Heating occurred continuously for 60 minutes with impedance data acquisitions and subsequent conductivity profiles reconstructed at 10 minute intervals. Overall, the results were quite satisfying and clearly illustrated the ability to localize a temperature rise within the phantom based on surface data augmented with internal measurements. At 30 and 60 minutes of heating, mean temperature errors ranged from 1°C to 1.6°C without internal recordings and 0.6°C to 0.7°C with internal data.

These laboratory experiments were followed by in vivo studies in animal and human subjects[51,52]. In the animal, heating took place on the thigh using a microwave spiral antenna operating at 433 MHz. A 32-electrode array arranged in a circumferential geometry was used to drive current and measure voltage during experiments. Electrodes were constructed using wet-etched printed circuit board techniques which were custom-sized based on pretreatment anatomical measurements. Temperature data was recorded along eight subsurface tracks with fiberoptic probes that were manually translated back and forth inside of catheters in 5 mm increments. Typical images and analysis of the animal encounters are described elsewhere[51].

Several similar clinical cases in humans have been reported by this group[51,52]. Superficial lesions were heated with the same 433 MHz spiral applicator. Electrodes were designed to lie flat on the body surface encompassing the tumor. As in the animal experiments, 32 electrodes were incorporated into a flexible array that was wet-etched on a thin polymide sheet to produce the required array pattern. Temperature data was recorded along two parallel tracks through the tumor every 2-3 minutes during the course of the therapy session and for several minutes at the end of treatment once power to the heating applicator had been turned off. Results from a typical clinical heating included reconstructed difference images over the time course of therapy. These images revealed a clear progression of the heating, then cooling which takes place as evidenced by the recovered increase, then decrease in electrical conductivity relative to baseline conditions. Areas of maximal change in conductivity correlated with the regions of highest measured temperatures during most of a treatment. Direct comparisons to measured temperatures were performed by translating the conductivity image changes into temperature estimates using an assumed temperature coefficient for tissue (nominally

2%/°C). These analyses demonstrated that temperature accuracies were 1.3°C on average, although maximum deviations of 10°C or more also occurred. In the areas of high error, increasing conductivity did not translate into increasing temperature, especially at the later time-points during treatment.

These results suggest that permanent change may have taken place in the heated tissue which was responsible for the nonlinear behavior in the imaged conductivity change. Cool down data also supported this hypothesis as the images produced sometime after power was turned off had conductivity distributions that did not return to their starting values. Further, the largest deviations from baseline correlated with those areas which sustained the most thermal dose. Data in the literature in mouse tumor models[53-54] also demonstrates the concept that linear variation in conductivity with temperature occurs during an initial heat-up phase in tissue, but gives way to nonlinear behavior as the amount of tissue injury from thermal exposure progresses during treatment. The idea that EIT imaging could follow this type of tissue injury progression due to thermal insult is intriguing and potentially more important and/or useful than monitoring temperature change, which is, in essence, an indirect vehicle for estimating the thermal dose delivered to tissue.

4. Illustrative Results

4.1 Hardware System Design

Considerable effort has been devoted to the realization of multi-channel, fixed frequency EIT hardware systems. Recent literature describes a number of EIT approaches which have focused on different aspects of instrumentation design. For example, Koukourlis et. al.[55] constructed a 32-electrode, 25 KHz device which emphasized data acquisition techniques. Smith et. al.[56] realized a 16-electrode, 20 KHz system with a design for achieving real-time imaging speeds. Cook et. al.[39] also developed a real-time imaging system consisting of 32 electrodes operating at 30 KHz but strove to achieve true 16-bit measurement precision as well. Comparisons have been made of these instruments across a number of hardware performance benchmarks relative to a system recently reported by Hartov et. al.[57]

The Hartov design includes a continuously-selectable driving frequency up to 1 MHz, either voltage or current source modes of operation and simultaneous measurement of both voltage and current on each channel in either of those driving configurations. VDC signal-to-noise ratios of 75-80 dB have been achieved with the noise floor for AC signals near 100 dB below the applied signal strength at 10 KHz and 60 dB down at 1 MHz. The added benefit of being able to record multi-spectral information on source and sense amplitudes and phases has also been realized. Phase sensitive detection and multi-period undersampling techniques have been deployed to ensure measurement fidelity over the full bandwidth of the system.

Figure 2 shows a photograph of this hardware realization. It currently consists of 32 channels multiplexed and controlled by a 200 MHz Pentium II PC via a 32-bit digital I/O board. Each channel is individually programmed with 12-bit accuracy to produce a given amplitude, sinusoidal signal ($\pm$ 12 V, $\pm$ 50 mA max). A reference sinusoid is produced at user-defined frequencies (DC to 1 MHz in 625 Hz increments) by a 12-bit, 40 MHz D/A waveform generator. Relays are used to switch separate voltage or current-source stages to the output for voltage or current modes of operation. A 16-bit, 200 KHz sampling rate A/D is used to digitize and record the measurements. Unlike many EIT systems, the measured signal amplitude and phase is not provided through hardware, but rather the voltage drop is detected across a sense resistor and a digital lock-

in amplifier algorithm is implemented in software to extract the signal amplitude and phase at the frequency of interest.

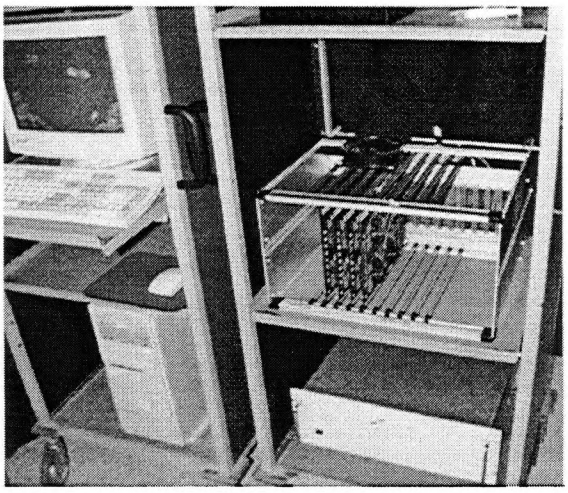

Figure 2: Photograph of the hardware system reported by Hartov et al.[57]

To maintain the integrity of the discretized waveform in terms of preserving its spectral content, the Nyguist sampling rate (twice the highest frequency) must be obeyed. A/D boards typically possess analog bandwidths that are 5 to 10 times higher than their highest sampling rate. To take advantage of this bandwidth an undersampling scheme is realized that increases the overall effective sampling rate. If the ratio of the sampling frequency to signal frequency is reduced to mutually prime factors that ratio represents the number of unique samples that are recorded. If this sampling rate is too high for the sampling rate of the A/D board it can be reduced by collecting the desired number of samples over more than one period of the sampled waveform. Hence, the same effective sampling rate can still be achieved, but the samples occur out of order. Figure 3 illustrates the point. The faster sampling rate is sufficiently high to capture the desired signal with the samples recorded in their natural order as shown. The slower sampling rate, on the other hand, requires two periods to complete a single cycle of the signal sampling. When these samples are presented in their natural order they produce the aliased waveform appearing in Figure 3. However, they contain the identical set of sampling positions within the signal period as those produced by the higher sampling rate and can, therefore, reproduce the sampled signal of interest provided they are properly ordered.

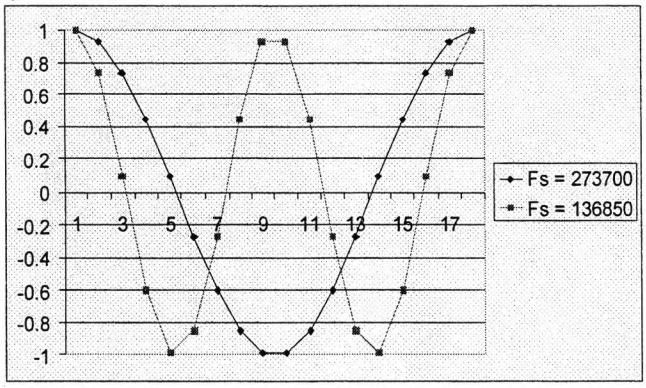

Figure 3: . A 16,100 Hz signal sampled at two rates with samples plotted in order of acquisition.

This method of selecting a sampling frequency is much faster than skipping whole numbers of signal periods in order sample at allowable intervals. The cycle-skipping technique consists of waiting a sufficient number of cycles plus the effective sampling period in order to acquire the samples in the correct order and with an effective

sampling rate which is much higher than that possible by direct, single-period sampling. Figure 4 demonstrates the cycle-skipping approach. In this case, the real sampling period, T_S, is the sum of some number of full signal cycles (T_{sig} in Figure 4) plus the effective sampling period T_e in Figure 4). This cycle-skipping strategy can be more than an order of magnitude slower than the multi-period scheme described in Figure 3.

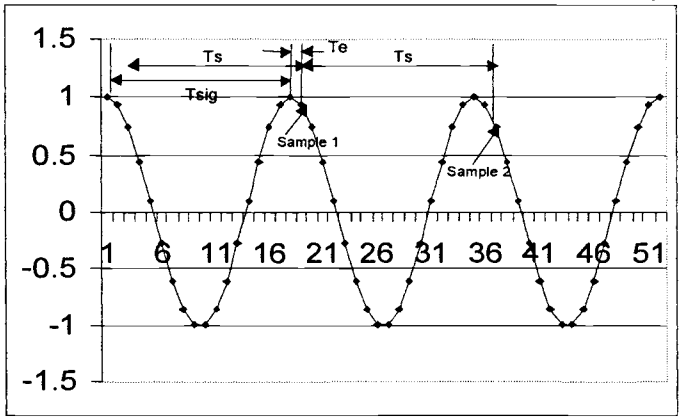

Figure 4: An illustration of multi-period undersampling using the cycle-skipping technique

4.2 Software Interface

The interface software developed by Hartov and colleagues involves the integration of several components including the waveform generator and A/D board which are operated through software libraries provided by the manufacturer. The customized channel module boards, on the other hand, require custom low-level drivers for the digital interface. Control instructions originate with the user and eventually reach the EIS hardware whereas measurement data flows the electrodes, passing through the data acquisition subsystem and ending with the control program where it can be used for image reconstruction.

The majority of core functions contained within the software reside in a special library known as Active X Control or OCX. This implementation allows a variety of commercial and custom programs to use Active X controls to extend their functionality. The OCX does not provide a user interface per se, but allows the algorithms in which it is embedded to serve as the vehicles for user inputs. Written in C++, the OCX is arranged in a hierarchical manner with high level functions located at the top of the hierarchy. The commercial device drivers at the bottom of the hierarchy are hidden behind generic interface objects so that the driver and its associated hardware may be changed without affecting any existing code. The custom software that drives the EIS channel boards uses a similar hierarchical structure to isolate hardware-related algorithms in order to limit the amount of code that must be rewritten when the hardware is modified or updated.

The primary user interface to the hardware system provides a control panel that allows digital servicing of all of the functions of the hardware system. An on-screen view of this control-panel is provided in Figure 5. This interface permits complete manual control of each channel. For example, the horizontal sliders in the figure allow independent voltage scaling for each channel. The software converts the position of the sliders to a 12-bit interger that the embedded Active X control then loads directly onto the channel board DAC through the digital electronics interface. As shown in the figure, the user can also select between an applied voltage or an applied current. The vertical

slider located along the right edge of the control panel allows the user to select a particular readback channel.

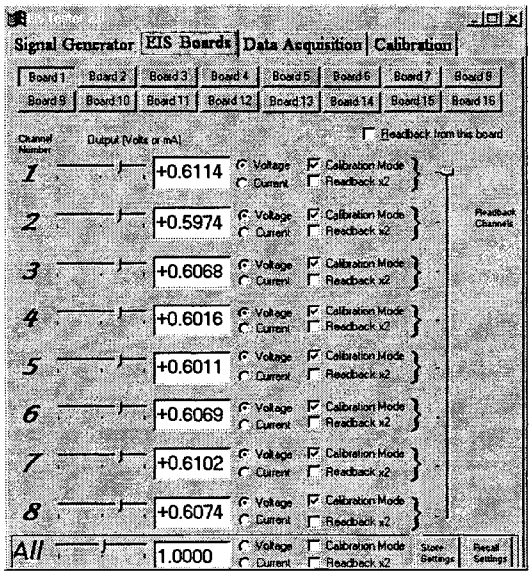

Figure 5: Manual Control Panel

The software also provides a control panel that automates data acquisition as shown in Figure 6. By engaging the button labeled "Acquire Data," the user may recorded and display a measurement. The program shows the measured amplitude and phase, real and imaginary components of the current and voltage or the two-element RC-equivalent load on each channel. A sequence of recordings involving all available channels (or any subset thereof) can be encoded, and the software will automatically select the appropriate, user-specified scaling at each electrode. If the user selects the button labeled "Run Experiment," the software will prompt the user for experimental parameters and then perform a series of data acquisitions. For each acquisition, the voltage or current amplitude at each electrode will be automatically set and recorded measurement information will be stored for subsequent numerical processing.

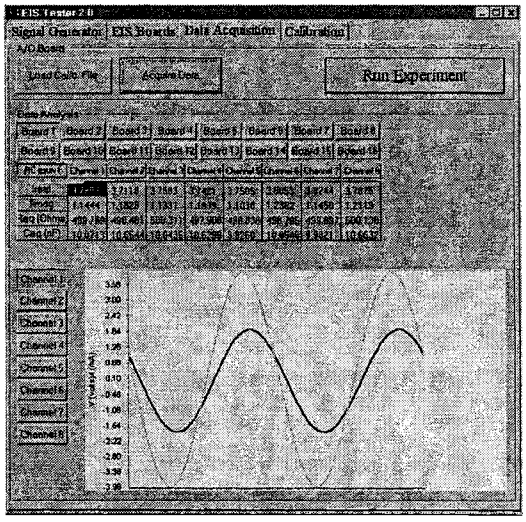

Figure 6: Automatic Control Panel

4.3 Phantom Experiments

Typically, initial imaging system characterization and calibration is performed in phantoms prior to progressing to in vivo conditions. In this regard, saline filled tanks or agar objects that contain contrasting inclusions are used to evaluate imaging system performance. Figure 7 shows a schematic of a phantom imaging experiment involving a saline tank with a single embedded target surrounded by 32 peripherally-located electrodes. Recently, Kerner et. al.[58] have used this arrangement to assess the image quality of reconstructions obtained from data collected with the Hartov et. al.[57] EIS instrumentation. Here, a summary of this experience is reported as a representative example of the kinds of images and resolution measures that can be obtained with electrical impedance imaging.

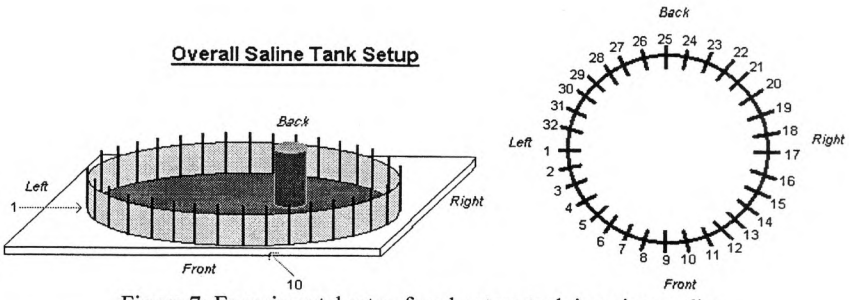

Figure 7: Experimental setup for phantom tank imaging studies

The tank used by Kerner was machined from a section of plastic pipe 20 cm in diameter and 6 cm tall where a circular Lucite base was attached and leak-proofed. Thirty-two 1 mm thick line electrodes were equally-spaced around the tank periphery. These electrodes were common iron paper clips snapped along the side of the tank. Approximately 70% of the straight portion of the paper clip was submerged in saline with the remaining round part hung over the top and outside of the tank for support and electrical connection to the hardware. The tank was filled to 4 cm height with 0.9% agueous NaCl solutions. Conducting and nonconducting test objects of various diameters (0.32, 0.64, 0.95, 2.54 and 3.4 cm) were placed in the tank at increasing depths (1, 2, 4 and 8 cm) from the tank surface. A full suite of imaging experiments were conducted for all five target sizes at each of 4 depths for both the conducting and nonconducting objects. Conductors were brass cylinders while nonconductors were solid nylon rods. Data was acquired at 10 frequencies and generally took about 3.5 minutes.

All the EIS images reported here display conductivity (S/m) as a function of position (x, y axes are in meters). In Figure 8, the absolute conductivity image of a blank tank, of one target 2 cm from electrode 12 and of two targets 2 cm in depth (from electrode 10 and electrode 26) are shown at 10 kHz. The targets were 3.4 cm wide nylon nonconductors and brass conductors. For the most part, the σ values recovered are physically meaningful. In these images, the background is determined to have a conductivity ~ 2 S/m which was close to the actual value of 1.98 S/m. The nonconducting object in the images appears to have a conductivity near 0 S/m which is also close to the actual value of ~$1x10^{-9}$ S/m. The conducting object appears to have a conductivity ~3.7 S/m which is far below the actual value of 1.43 x 10^{8} S/m. The slight inhomogeneities around the periphery of the images correspond to artifacts due to the electrodes.

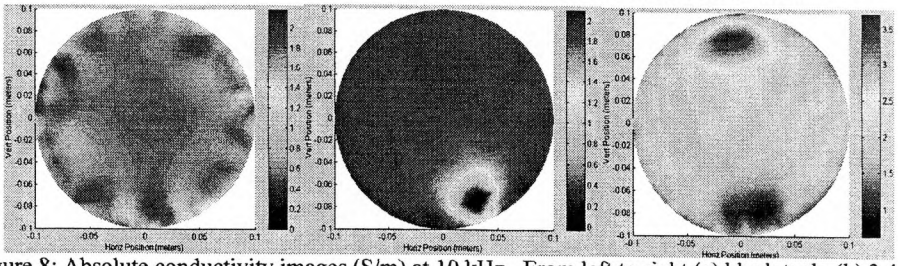

Figure 8: Absolute conductivity images (S/m) at 10 kHz. From left to right (a) blank tank, (b) 3.4 cm wide nonconductor by electrode 12, and (c) 3.4 cm wide nonconductor by electrode 10 and 3.4 cm wide conductor by electrode 26.

Figure 9 shows how the resolution of targets increases with frequency. In this figure, all of the images depict absolute reconstructions of a 3.4 cm wide conductor in the same position, i.e. 2 cm from electrode 21. At 10 kHz, the background appears most

inhomogeneous and there is a pronounced halo around the target. At 125 kHz, there is less of a halo around the target. At 950 kHz, the halo is least pronounced and the saline background appears most homogeneous.

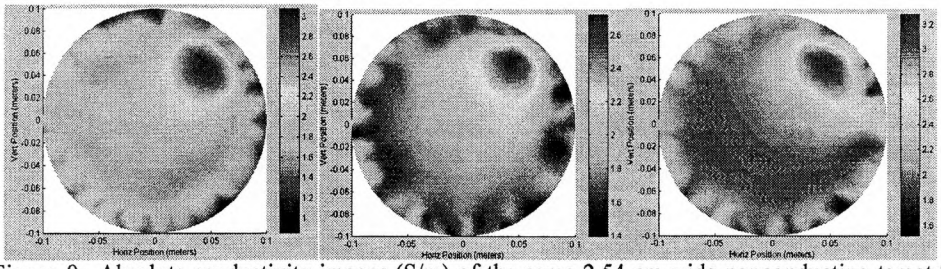

Figure 9: Absolute conductivity images (S/m) of the same 2.54 cm wide nonconducting target 2 cm from electrode 10 at 2 frequencies. From left to right (a) 10 kHz, (b) 125 kHz, and (c) 950 kHz.

Figures 11 and 12 indicate that difference images enhance the contrast relative to absolute images at a given frequency. In this case, a 2.54 cm wide conductor was placed 2, 4, and 8 cm from electrode 10. The electrode artifacts were consistently attenuated in the difference images. When the object is 2 cm from the edge, one can localize the target in both the absolute and difference images. With the object 4 cm from the edge, one barely detect the presence of the target in the absolute image while the target appears very clearly in the difference image. Finally, with the object 8 cm from the edge, one can vaguely detect the presence of a target within the difference image (albeit the target's edges are poorly defined) while no target is discernable in the absolute image.

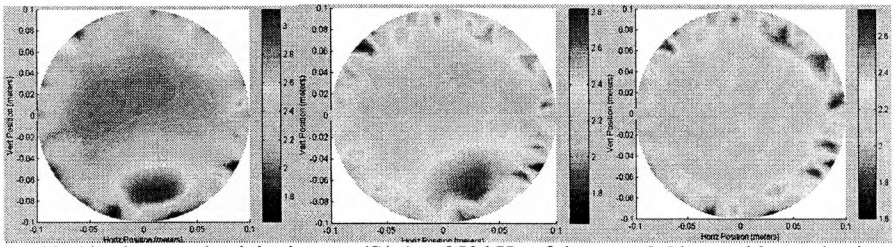

Figure 11: Absolute conductivity images (S/m) at 950 kHz of the same 2.54 cm wide conducting target at 3 positions. From left to right (a) 2 cm, (b) 4 cm, and (c) 8 cm from electrode 10.

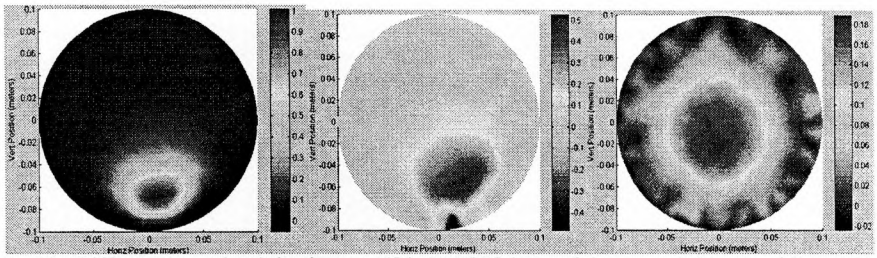

Figure 12. Difference conductivity images (S/m) at 950 kHz of the same 2.54 cm wide conducting target at 3 positions. From left to right (a) 2 cm, (b) 4 cm, and (c) 8 cm from electrode 10.

Kerner defined this type of blurry difference image as the threshold for object detection (i.e. maximum discernable depth) since it still could be distinguished from difference images of successive blank tanks. Figure 13 graphically summarizes the imaging system's resolution at 950 kHz. The difference images of conductors have the largest maximum discernable depth. In general, wider objects can be detected at greater depths. Also, difference images have greater discernable depths than their absolute image

counterparts. Conductors have slightly larger discernable depths than nonconductors of equivalent size. The maximum discernable depth levels-off at 8 cm which is 2 cm away from the tank's center (10 cm). This implies that objects must be greater than 2.5 cm in width to be detected in the center of this phantom.

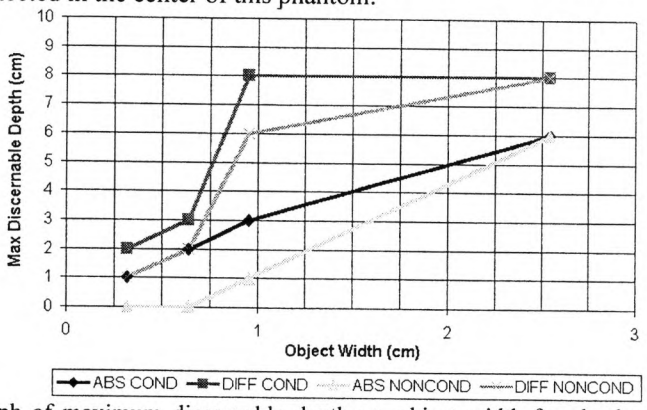

Figure 13: Graph of maximum discernable depth vs. object width for absolute and difference images of conductors and nonconductors at 950 kHz.

As a final example, Figure 14 shows an in vivo permittivity image of the forearm. This result is rather impressive. First, the reconstruction recovers the permittivity response of tissue. The major muscle masses are evident in the image along with the bone and surrounding soft tissue.

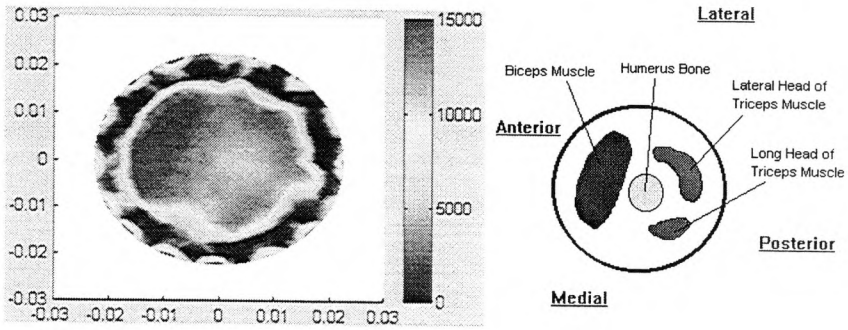

Figure 14: In vivo EIS image of the human arm.

5. Active Microwave Imaging

5.1 Physical Principles

Active microwave imaging in the medical context exploits propagating electromagnetic fields over the spectral range of hundreds of MHz to several GHz. Because the illuminating signals radiate from their source, direct contact with the tissue is not necessary, although a coupling or matching medium is generally required. Typical radiators for medical microwave imaging have included waveguides, planar antennas and dipole or monopole arrays. In contrast to EIT where direct signal sampling is used, some form of heterodyning is common because the tissue interrogation frequencies are too high for plug-in A/D sampling boards. Heterodyne technique mixes two signals of nearly the

same frequency to produce their sum and difference spectral components which are appropriately filtered to provide the intermediate frequency (IF) which can be accurately digitized with off-the-shelf A/D cards.

In the spectral range of interest, electromagnetic fields interact with tissue in three ways. First, they induce a conduction current through the creation of ionic flow resulting from the forces exerted on unbound charges (ions) within the tissue. Second, alignment and oscillation of naturally existing dipolar molecules (e.g. water) occurs with the applied field. Depending on the size of the molecule and the frequency of the stimulus, these dipoles either completely or partially polarize in the sense that they make complete or partial rotations in synchrony with the oscillations in the applied field. Third, naturally nonpolar molecules can become polarized through small movements in bound charges of opposite sign caused by the alternating forces created by the applied field. Clearly one of the dominant effects is the dipolar orientation of water in tissue, but significant conduction currents can be generated and tissue macromolecules such as proteins and organelles can also undergo dipolar reorientation as well.

Active microwave imaging has been considered to have the potential of being a powerful medical imaging modality for many years[59-63], largely based on a substantial amount of data which has consistently shown that the electrical properties of tissues over the frequency range of hundreds of megahertz to several gigahertz can vary an order of magnitude or more[1-3,12-14]. For example, the relative permittivity can range from 5 to 80 while the conductivity can extend from 0.02 to 1.9 siemens/meter over the frequency band 300 - 1100 MHz. In terms of soft tissue, this provides an electrical property contrast of 20:1 or more as compared to the contrast levels of only a few percent which are available with other imaging modalities. While initially viewed as a low-cost alternative to CT, microwave imaging will likely play its largest role in specialty application such as thermal imaging for therapy monitoring, assessment, and control where electrical conductivity is known to change with temperature at a rate of several percent per degree of temperature rise[1-3].

At microwave frequencies, electromagnetic field interactions with tissue are well described by Maxwell's equations for time-harmonic sources

$$\nabla x E = i\omega\mu H \tag{5a}$$

$$\nabla x H = -i\omega\varepsilon^* E \tag{5b}$$

$$\nabla \cdot E = \rho \tag{5c}$$

$$\nabla \cdot H = 0 \tag{5d}$$

where E and H are the electric and magnetic fields, ρ is the charge density, ω is the angular frequency of excitation, $i = \sqrt{-1}$ and ε^* is the complex-valued permittivity whose real part is proportional to the electrical permittivity, ε, and imaginary part is proportional to the electrical conductivity, σ. Typically, either E or H is eliminated in terms of its counterpart by combining the first order curl equations into a second order system, which for E in tissue would be written as

$$\nabla x \nabla x E - k^2 E = 0 \tag{6}$$

where $k^2 = \omega^2 \mu \varepsilon^*$.

In general, two serious difficulties have retarded the development of active microwave imaging in the medical context. The first is related to equation (6) which indicates that image reconstruction cannot realistically proceed in terms of the classical projection-type algorithms which have dominated tomographic medical imaging[63-64]. Early attempts at medical microwave imaging were not overly successful because most

image reconstruction efforts adapted back-projection or back-propagation algorithms that were well-known in CT. These approaches may have been natural at the time because they were readily available and required relatively modest computational resources. However, they were fundamentally inadequate because solution to (6) in heterogeneous tissue at the frequencies of interest (i.e. below 3 GHz) reveal that a significant amount of scattering and diffractiton exist rendering straight-line back-projection or back-propagation algorithms of marginal utility in microwave imaging applications[65].

The second major technical difficulty with microwave imaging is that data acquisition is compromised by the significant tissue attenuation of the signals to be recorded and the potential for measurement artifacts arising from undesired scattered fields and cross-coupling between transmit and receive elements within an imaging array. The signal attenuation issue was exacerbated by the fact that early estimates of achievable spatial resolution suggested that illumination frequencies needed to be in the low gigahertz[62]. The limited penetration depths of electromagnetic signals at these frequencies dictated that either unrealistic dynamic ranges had to be achieved or tissue depths had to be restricted to clinically uninteresting dimensions.

Methods and systems evolved toward utilizing more appropriate but still highly restrictive diffraction theory approximations[60, 66-68]. Specifically, Born approximations became the norm which develop the scattered field as an integral equation solution to (6), except that rather than using the total field modulated by the contrast function in the integral equation kernal, the known incident field is used instead. In effect, this assumes that the medium does not significantly distort the incident field in order to produce its scattering response; that is, the region of interest is weakly scattering. This is clearly a poor assumption for biological tissue and not surprisingly, image reconstructions in biological media which were based on Born approximations were not very satisfying even though this approach tried to capture some of the physics embodied in equation (6). Some qualitative images of low contrast biological stimulants were produced which did demonstrate proof-of-principal results that were important advances in the evolutionary growth of active microwave imaging[61-61, 65-69].

With the advent of considerably more computational power being available at a modest cost, image reconstruction algorithms which model the full electromagnetic interactions occurring in the body during microwave illumination have begun to appear[70-78]. These methods have generally been two-dimensional in which case the model described by equation (6) reduces to the classical Helmholtz equation in the field component perpendicular to the imaging plane:

$$\nabla^2 E_z + k^2 E_z = 0 \qquad (7)$$

where the subscript z designates this direction. As with model based imaging for EIT, schemes which repetitively solve (7) to estimate the electrical properties embodied in the complex-valued wavenumbers, k^2, appear to hold the most promise as image reconstruction approaches for active microwave imaging as well. These methods also use parameter estimation methods to find the electrical property profile which optimizes the data-model match between computed and measured field distributions. As with EIT, least squares objectives are typically used as the optimization criterion[73,75,77-78]. Commonly, computational strategies such as method of moments and finite elements have been used to discretize (7). Property estimation based on iteratively minimizing the squared error between computed and measured electric fields require computation of the derivatives of the solution to (7) with respect to each property parameter. Analogously to EIT, basis function expansion of k^2 as

$$k^2 = \sum_{\ell=1}^{N} k_\ell^2 \varphi_\ell$$

allows convenient differentiation of (7) with respect to each successive term in the sum yielding

$$\frac{\partial}{\partial k_\ell^2}\left[\nabla^2 E_z + k^2 E_z\right] = \nabla^2 \frac{\partial E_z}{\partial k_\ell^2} + k_\ell^2 E_z + k^2 \frac{\partial E_z}{\partial k_\ell^2} = 0 \tag{8}$$

which can be rewritten as

$$\nabla^2 E' + k^2 E' = -k_\ell^2 E_z \quad \text{where } E' = \frac{\partial E_z}{\partial k_\ell^2} \tag{9}$$

Equation (8) is identical to (7) except for the inhomogeneous term on the right hand side which can be viewed as the known source for each derivative calculation since (8) is computed for the current estimate of the electrical properties after the field equation (6) has already been solved. Again, the electrical properties are a nonlinear function of the external field values requiring iterative solution techniques involving the sensitivity matrix. The options which are available included both random processes[79-81] as well as deterministic techniques[76-78] as described above for EIT.

While further advancement is clearly needed, these model based approaches have laid a conceptual foundation for active microwave image reconstruction upon which microwave imaging can be soundly developed and elevated in vivo. They afford two significant advantages. First, unlike their predecessors, they are fundamentally unlimited by wavelength and contrast considerations because they are essentially near-field imaging techniques which are not constrained by conventional far-field diffraction-limit arguments, but rather are ultimately limited by signal-to-noise. This leads to the second advantage that lower frequencies can be utilized with these types of algorithms without severe degradation in resolution. Early estimates of optimal operating frequency for microwave imaging were driven by the diffraction limit which led to the need to design hardware systems functioning at 2-4 GHz. With the newer class of model-based image reconstruction algorithm, lower frequencies (below 500 MHz) can be used which reduce system dynamic range requirements and increase tissue depths that can be imaged without unduly compromising spatial resolution. Clearly, tradeoffs between wavelength dependent spatial resolution and imaging depth still exist, but the impact is diminished by these algorithms which offer operating points that can provide centimeter-scale spatial resolution over tissue regions on the order of cross-sectional body dimensions.

Unfortunately, these reconstruction methods are not without some drawbacks. They are computationally intensive with costs that escalate significantly with frequency. They have been studied to much greater extent in theory and have not been thoroughly characterized in the laboratory setting. They require information from complex data acquisition hardware that demands well designed circuitry and calibration which (i) eliminate stray radiation and cross-coupling between neighboring transmit/receive elements and (ii) provide high precision measurement of field amplitude and phase.

6. Historical Perspective

The proposition for using active microwave imaging for noninvasive thermal sensing began in earnest in the early 1980s[59, 63-64,69] when Bolomey and colleagues started developing a microwave camera. They envisioned a single microwave source, such as a horn antenna, transmitting GHz range signals received by an array of 32 small dipoles where a modulated scattering technique was used to extract the measured signal from

each dipole. In a thermal imaging experiment involving the heating of a 2 cm tube of water located in the middle of a 13 cm span from transmitter to receiver, the temperature was elevated in the tube from 25°C to 45°C. Difference images were shown[69] where temperature rise appeared as bright spots in the image. Spatial resolution was estimated to be 6 mm and temperature sensitivity to be less than 1°C. In parallel, theoretical work was going on trying to adapt the algorithms of CT scanning to the microwave case[63-64]. These approaches were natural at the time due to the fact that the algorithms were readily available and the computational costs tractable; however, they were fundamentally inadequate[65]. By 1986, there were several groups developing prototype microwave imaging systems and image recovery methodology[61]. For example, Larsen and Jacobi showed[82] some rather impressive microwave images of an ex-vivo kidney. Their microwave system consisted of a single pair of water-loaded transmitting and receiving antennas scanned in tandem through a water coupling medium. The image was formed from a 64 x 64 array of sampling positions spaced 1.4 mm apart where the insertion loss and phase shift was recorded at each point in the grid for a 3.9 GHz illumination signal. The scanning system provided both vertical and horizontal translation about the specimen to be imaged. Copolarized and cross-polarized data was recorded with the transmitting antenna always vertically polarized but the receiving antenna alternately polarized in the vertical and horizontal directions. Digital image processing of the measured data, for example, to interpolate it onto a 256 x 256 grid from the 64 x 64 measurement pattern using a cubic spline was involved but no formalized image reconstruction was performed. They found that their microwave images could sense internal kidney structural differences including the cortex, medulla and pelvis. Back projection methods were used to produce the images from the raw data collected by sensors scanned in a linear fashion.

More advanced systems were reported in the early 1990s with the annulus of waveguides reported by Jofre et. al.[66]. This scanner consisted of 64 elements in a circular array forming a 20 cm diameter. These radiating elements were electronically scanned, alternately as sources and receivers, to produce a complete set of response observations about the target zone. The system exploited a water coupling bolus. Several interesting results related to blood flow/volume and temperature elevation were shown. For example, a 3 cm diameter tube of heated water was placed off-set in a water tank and experiments were performed to estimate the temperature sensitivity of the system at 0.5°C.

A number of simulation studies investigating the potential of active microwave imaging for thermal sensing have also been conducted[74,83-89]. One such series of numerical experiments used an 8 cm circle region of water held at 37°C immersed in a 30 cm circle of background medium at 25°C. A localized temperature change inside the body was simulated by a 2 cm nonconcentric cylinder heated to 38°C or 41°C. Other experiments involved a model of the human pelvis and thorax[83]. Here, frequencies under study included 434 MHz, 700 MHz and 915 MHz where 64 antennas were evenly distributed on a 60 cm diameter array. Multiple heated zones having an increase in temperature of 1°C, 3°C and 5°C were considered in each body cross-section. In the case of the thorax, six heated zones showed that a 1°C rise was visible, although difficult to discriminate from other areas of increase within the image which were not heated and no quantitative assessments were provided.

A different strategy for microwave thermal imaging was adopted by Miyakawa in the early 1990s[65,85-86]. This scheme utilized a chirp pulse signal between 1-2 GHz to estimate temperature changes noninvasively. Transmitted signals were detected by a receiving array on the opposite side of the object where the beat signal between the incident and transmitted fields was produced by mixing. Only signal traveling along a straight path from transmitter to receiver was detected through spectral analysis of the beat signal which rejected the multipath components thereby allowing an image to be reconstructed easily using conventional x-ray CT algorithms. To estimate the spatial

resolution of the method, two 5.5 cm plastic cylinders filled with 0.2% saline were separated by distances of 3 cm, 1.5 cm, 1.0 cm and 0.5 cm. Based on these experiments, the spatial resolution was estimated to be 1.0 cm. Temperature studies were conducted in a phantom having three plastic cylinders filled with water which were heated 5°C above the background (0.4% saline solution), held at the background temperature and cooled to 5°C below the background. These temperature changes were found to be evident in the recovered images. Based on hardware signal-to-noise estimates, it was concluded that a temperature change of less than 3.3°C would be detactable.

In a series of papers reported by Meaney and colleagues, a system of monople antennas have been used to transmit and receive electric fields over the 300-900 MHz range for the purpose of active microwave imaging[87-91]. In this work both manually scanned single transmitter/receiver pair and multi-element fixed array hardware have been investigated. Single and multi-target phantom experiments have demonstrated that simultaneous absolute permittivity and conductivity images can be recovered which are quantitatively accurate with respect to the electrical properties[87-88]. Critical to this success has been the deployment of model-based image reconstruction techniques that account for the full near-field electromagnetic interactions which occur in tissue[78]. An extensive series of thermal imaging experiments have also been reported[92] in both simulated and laboratory systems. In numerical simulation, a precision of 0.02°C and an accuracy of 0.37°C has been found with the model-based approach. In the laboratory using a phantom consisting of a single-heated zone, temperature precision and accuracies have been 0.98°C and 0.56°C under selected circumstances. Results from the experience will be highlighted in subsequent sections of this review.

Other important active microwave imaging results have also been recently reported[93,94]. For example, a tomographic system consisting of 32 transmitters and 32 receivers, electronically scanned around a 36 cm cylindrical microwave chamber has been reported by Semenov and coworkers[93]. This system operates at 2.45 GHz, uses an incident electromagnetic field polarized linearly in the vertical direction relative to the imaging plane, and acquires all of the necessary data in less than 0.5 seconds. Experimental results from the system have suggested a spatial resolution of 1-2 cm and a contrast resolution of 5%. This same group has also developed iterative reconstruction algorithms[76] that have been evaluated with synthetic data.

Progress also continues to be reported by the Bolomey team[93,75]. Importantly, they have demonstrated quantitative reconstructions from experimental, multiview near-field data obtained with their planar 2.45 GHz active microwave camera. Iterative reconstruction using model-based optimization has been used where the method of moments serves as the computational engine. Test objects included contrasts of 0.8% and 40% and 3% and 150% in permittivity and conductivity, respectively, where either 15 or 30 views were used. Related studies involving the microwave scanner described by Jofre have also appeared.

7. Illustrative Results

7.1 Hardware System Design

In this section the hardware data acquisition of Meaney et. al.[87-90] is briefly summarized as representative of a state-of-the-art system. The design is constructed around a 32 channel transceiving network which operates over the spectral range of 300 -900 MHz. It exploits a single side-band heterodyne approach[87] where the continuous wave reference signal is modulated with an intermediate frequency (IF) using a single side-band, carrier-suppressed upconverter. The received modulated signal is then

compared with the reference through a single mixer. The resulting IF was initially read by a commercial grade lock-in amplifier which extracted the in-phase and quadrature components and performed the A/D conversion. Later versions of the system eliminated the external lock-in amplifier in favor of direct A/D board sampling coupled to a software implementation of phase sensitive detection. This advance not only consolidated system components into the controlling PC but also significantly sped-up data acquisition. A complete set of imaging data involving 32 transmitter positions can be collected in under 5 seconds. High performance measurement precision is also maintained through a signal dynamic range of 130 dB. Figure 15 show recent photographs of this system. The microwave circuitry associated with the switching matrix can be seen along with connections to an antenna imaging array.

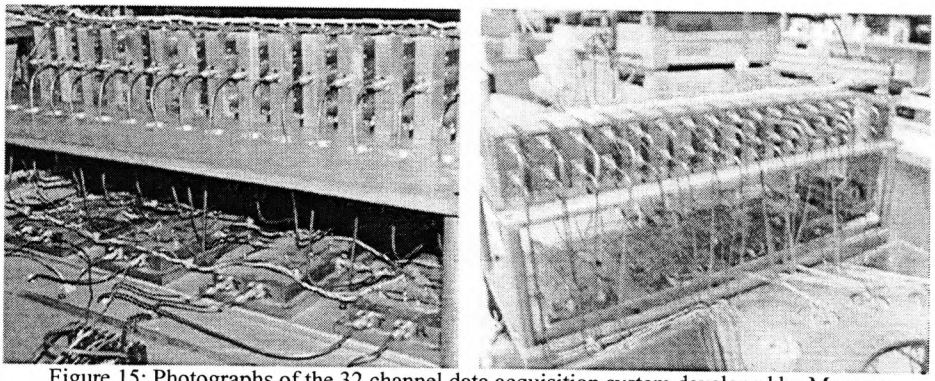

Figure 15: Photographs of the 32 channel data acquisition system developed by Meaney

The transmitting and receiving elements are simple monopole antenna designs which were constructed by simply exposing a quarter-wavelength (in the medium of interest at 500 MHz) of the center conductor (physical length of 2.5 cm) of a semi-rigid coaxial cable. While this type of antenna is notorious for exciting currents along the outside of the coaxial cable in a low-loss environment such as air, the high attenuation of the coupling saline solution significantly dampens this effect to the extent that the antenna return loss is quite smooth over the broad bandwidth of 300-900 MHz. The monopole transceiving array provides the physical advantage of eliminating more bulky elements such as waveguides or patch antennas in favor of a single type of simple antenna component which is conducive to a fixed array data acquisition design that may become important in realizing clinically viable systems. Figure 16 illustrates a typical 32 antenna array of monopole elements distributed on a 26 cm radius.

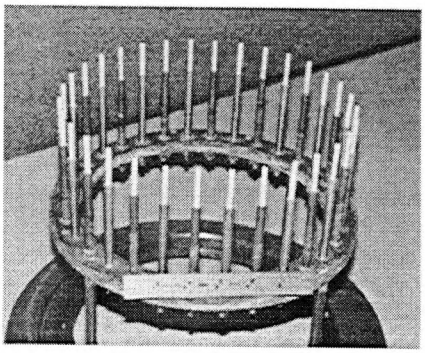

Figure 16: Fixed-position, 32 element monopole antenna array

A number of operational issues surround the use of a monopole transceiving design within the context of near-field imaging and the performance of such a system vis-à-vis other approaches needs to be investigated. In particular, the level of data-model match which can be achieved with computational solutions that form the basis for image reconstruction with the monopole system must be studied. In

addition, the extent to which the isotropic radiation pattern of the monopole element influences reconstructed image quality must be understood. Meaney and colleagues[89] recently explored these issues by comparing monopole and waveguide imaging systems.

They found a new calibration method that leads to improvements which are independent of the type of radiator used. Specifically, data-model match was found to increase by 0.4 dB in magnitude and 4° in phase for monopoles and by 0.6 dB in magnitude and 7° in phase for waveguides (on average) on a per measurement basis when the new calibration procedure was employed. Enhancements were also found in the reconstructed images obtained with the monopole system relative to waveguides. Improvements were observed in (1) the recovered object shape, (2) the uniformity of the background, (3) the sharpness of edge detection, and (4) the accuracy of the target property value recovered. Analyses of reconstructed images also suggested that there was a systematic decrease of approximately 10% in the reconstruction errors for the monopole system over its waveguide counterpart in single-target experiments and as much as a 20% decrease in multi-target cases. Results indicate that these enhancements stem from a better data-model match for the monopoles relative to waveguides which is consistent across the type of calibration procedure used. Comparisons of computations and measurements showed an average improvement in data-model match of approximately 0.25 dB in magnitude and near 7° in phase in favor of the monopoles in this regard. Beyond these apparent imaging performance enhancements, the monopole system offers economy-of-space and low construction-cost considerations along with computational advantages which make it a good choice as a transceiving element around which to construct a clinically viable, near-field microwave imaging system. Figure 17 shows sample reconstructed images for a 4.3 cm diameter bone/fat equivalent cylinder separated by 1.4 cm from a 3.8 cm diameter plexiglas cylinder filled with 0.3% NaCl agar gel where both monopole and waveguide systems have been used. Included in the results are longitudinal transects through images displaying the reconstructed property profiles. These transects make it clear that the monopole images are better.

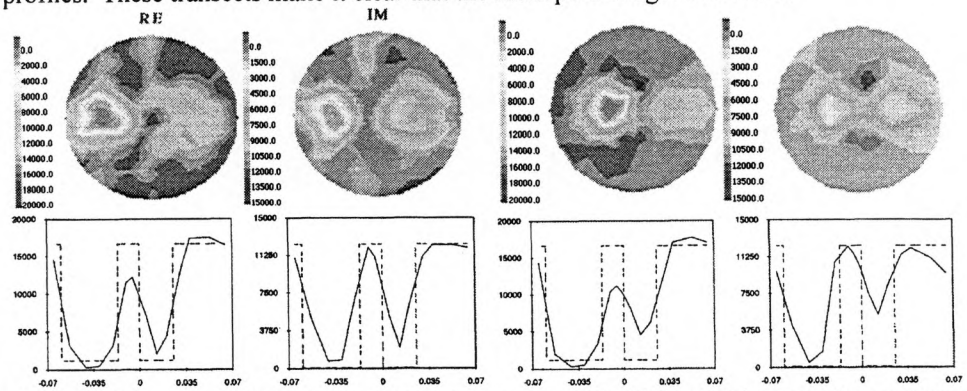

Figure 17: Reconstructed monopole (left pair) and waveguide (right pair) images of a two-target distribution with transect plots illustrating the exact and recovered property profile.

Another important aspect of microwave imaging hardware is that fixed array systems with multi-sensor data acquisition can suffer from nonactive antenna element interactions which cause distortions in the measurements. To address this problem Paulsen and Meaney[95] have developed a nonactive antenna compensation scheme which can be incorporated into model-based near-field microwave image reconstruction methods. The approach treats the nonactive members of the antenna array as impedance boundary conditions applied over a cylindrical surface of finite radius providing two parameters, the effective antenna radius and impedance factor, which can be determined

empirically from measured data. Results show that the effective radius and impedance factor yield improved fits to experimental data in homogeneous phantoms where measurements were obtained with and without the presence of the nonactive antenna elements. Once deduced, these parameters are incorporated into the nonactive antenna compensation model and lead to systematic data-model match improvements in heterogeneous phantoms.

While the improvements afforded by the nonactive antenna model are small on a per measurement basis, they are not significant. As demonstrated by Meaney et. al.[91] incorporation of the nonactive antenna compensation model produces significantly higher quality image reconstructions from measurements obtained with a fixed array data acquisition system over the spectral range of 500-900 MHz. Improvements were found to be most dramatic for inclusions located in near proximity to the antenna array, itself, although cases of improvement in the recovery of centered heterogeneities were also evident. Increases in the frequency of illumination yielded an increased need for nonactive antenna compensation. Quantitative measures of recovered inclusion shape and position revealed a systematic improvement in image reconstruction quality when the nonactive antenna compensation model was employed. Improvements in electrical property value recovery of localized heterogeneities were also observed. Figure 18 shows reconstructed images at 900 MHz of a centered and offset bone/fat equivalent inclusion with and without the nonactive antenna compensation model. In this case there is a clear improvement in both the near-edge target shape as well as its shape and size when located in the central portion of the image zone.

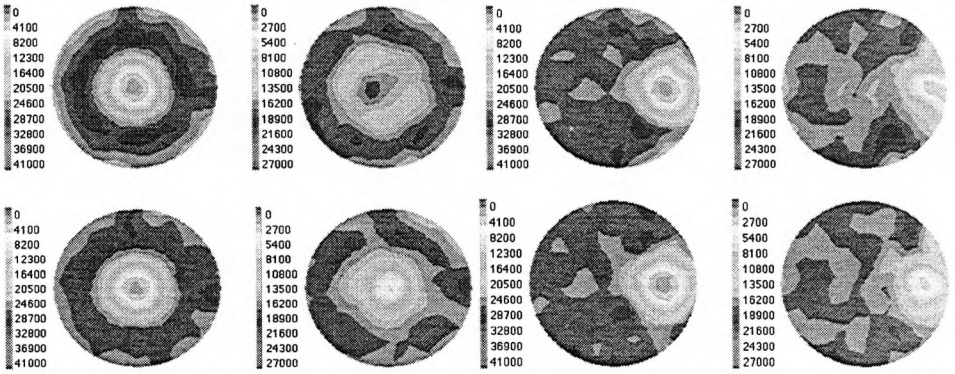

Figure 18: Images reconstructed with no compensation (top row) vs. compensation (bottom row) for centered and offset single bone/fat targets illuminated at 900 MHz.

7.2 Static Phantom Studies

This section focuses on representative experiments in terms of both static target imaging. Clearly, prior to investigating the more complex problem of thermal imaging, it is important to establish the degree to which quantitative, spatially-resolved electrical property images can be obtained since these form the foundation from which thermal estimation takes place. Figure 19 illustrates a typical image pair of a 4.3 cm bone/fat target and a 2.5 cm bone/fat target separated by 1.7 cm. The reconstruction has been obtained from laboratory data collected at 700 MHz. The images are of high quality, resolving the targets in both electrical property quantities. Most importantly, as shown by the transects through the images, the recovered property values for the background and target regions are quantitative. Figure 20 shows a related three target case where a 3.8 cm plexiglas cylinder of deionized water, a 4.3 cm bone/fat cylinder and a 2.5 cm

bone/fat cylinder are located in a clockwise order beginning at 10 o'clock. All of these objects have been placed in a muscle-like background region illuminated at 700 MHz.

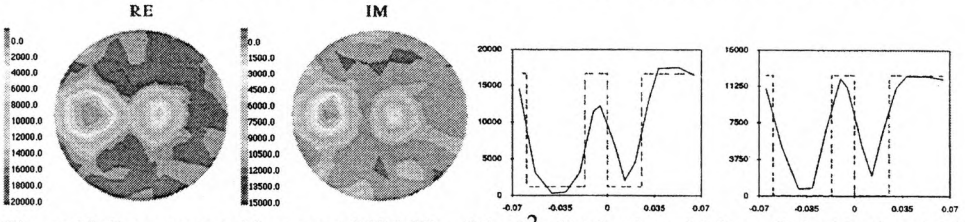

Figure 19: Reconstructed images at 700 MHz of the k^2 distribution of 4.3 cm (left object) and 2.5 cm (right object) fat/bone equivalent cylinders separated by 1.7 cm. Exact and reconstructed electrical property profiles along transects through the images also shown.

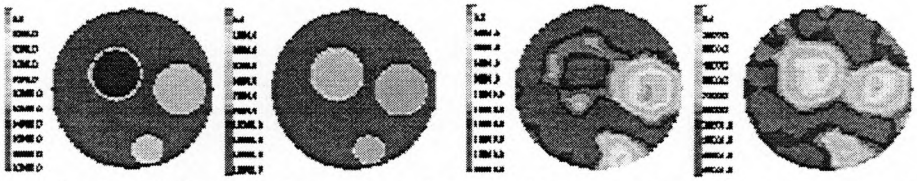

Figure 20: Exact (left pair) and reconstructed (right pair) images of a three target configuration illustrating low and high contrast materials in the real (left) and imaginary (right) components of the electrical property distribution.

The thin plexiglas ring is readily visible in the real part of the image (left side) along with the other targets and their respective low (real part of deionized water) and high (imaginary part of bone/fat) contrasts with the muscle-equivalent saline background. It is very encouraging to find that the presence of the plexiglas ring appears in the image as well as the fact that the material inside the plexiglas cylinder has essentially no contrast with the surrounding medium in the real part (left) of the image, but high contrast in the imaginary component (right) of the image. The wall thickness and large contrast (37:1 in the real part and 100:1 in the imaginary part) make it difficult to recover the material properties of the plastic exactly; however, the general shape and location of the wall are discernible and its lower electrical properties are evident. The recovered ring is more pronounced in the real part of the image due to the lower contrast level of the plastic with materials both inside and outside of the cylinder (compared to imaginary).

7.3 Thermal Imaging Experiments

A variety of thermal imaging experiments involving a controlled heated zone where changes in electrical properties have been monitored during the heating process are reported in Chang et. al.[92]. Example results presented here are intended to illustrate that microwave imaging can dynamically monitor the small changes in electrical properties which are related to local temperature elevation. An extensive series of simulation studies have been conducted in order to define and evaluate the parameters which determine best-case thermal imaging performance. Specifically, the baseline contrast of the target zone to be heated has been varied between 0.3% and 1.2% NaCl relative to a 0.9% NaCl background prior to heating over a range of temperature spanning 25°C-45°C. Values of reconstructed electrical conductivity have been mapped to temperature using measured data for the electrical properties of the target saline at each of the imaged temperature levels. Image reconstructions have been obtained for illumination frequencies of 300, 500, 700 and 900 MHz. Figure 21 illustrates a typical result from this effort for the 1.2% NaCl initial concentration contrast at 700 MHz. Transects through the

Figure 21 images show the quantitative nature of the electrical property recovery relative to exact values as a function of temperature rise.

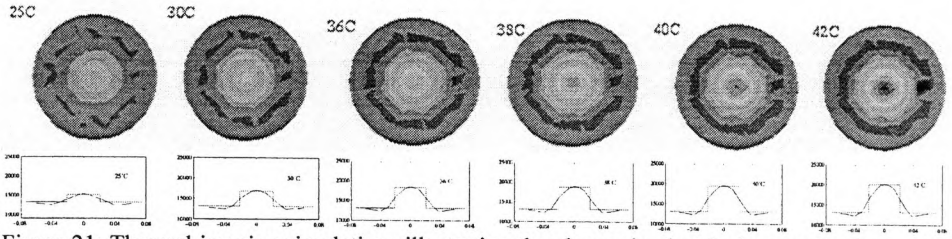

Figure 21: Thermal imaging simulations illustrating the change in electrical properties in a central heated zone. Transects through the imaging domain show profiles of exact (dotted line) and reconstructed (solid line) property values.

Linear fits to both measured and simulated data relating electrical conductivity (imaginary component of the recovered image) to temperature have been obtained for the three target saline concentrations. Precision in this data has been estimated by evaluating the average deviation of the data points from the best-fit line in each case. Accuracy has also been estimated in a similar fashion by determining the averaged error between the measured and reconstructed values using the center point of the target zone over the full temperature range of 25° C-42°C. The results are encouraging and show that the average precision over the three saline concentrations is approximately 0.1°C-0.2°C whereas the corresponding average temperature imaging accuracy is 0.6° C-0.7°C. A similar series of experiments have also been conducted in the laboratory where initial saline concentration contrast between the heated zone and the background has been varied and the frequency of data acquisition has ranged from 300-900 MHz. Figure 22 presents an interesting case where the heated zone is a 5 cm diameter carbon-doped PEMA cylinder with 0.4 mm wall thickness which has been placed adjacent to an unheated 2.5 cm bone/fat object.

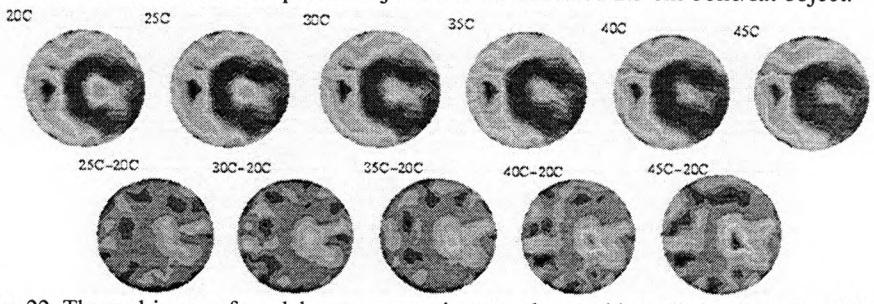

Figure 22: Thermal images from laboratory experiments where a thin-walled carbon-doped PEMA cylinder containing 0.3 % NaCl is heated while positioned next to an unheated fat/bone target embedded in a muscle-equivalent saline background. Sequences of absolute (top row) and difference (bottom row) images are shown. A clear progression of electrical property increase is observed inside the PEMA cylinder where the saline concentration is heated.

The carbon-doped PEMA cylinder has higher electrical properties than the 0.9% saline background region. The top row of images presents the absolute reconstructions of the imaginary component of the electrical properties for increasing temperatures of the 0.3% saline inside the PEMA shell. The unheated bone/fat target, the heated saline, the PEMA shell and the unheated saline background are all apparent in these images. The bottom row of images shows differences taken at each elevated temperature with the 20°C baseline. In the difference images, the bone/fat object along with the carbon-doped PEMA shell disappears since their temperatures do not increase. Analysis of the

precision and accuracy of this and other thermal imaging experiments performed in the laboratory are reported in Chang et. al.[92]. The results show that a best case temperature precision of 0.98°C and accuracy of 0.56°C can be achieved in the laboratory. The precision and accuracy averaged over the full range of frequencies and electrical property contrasts that have been considered suggests values of 2°C and 1.4°C, respectively, for the current microwave imaging system realization.

The potential benefits of including apriori structural information in the thermal image reconstruction process has also been explored as this information could become available in the context of therapy monitoring and assessment when high resolution preprocedure imaging is already part of standard practice. The series of reconstructed images in Figure 23 shows the improvement in thermal accuracy gained by providing apriori information to the image reconstruction. Using the 32 channel acquisition system of Meaney et. al.[90] with a 24 cm diameter imaging region, a two-target phantom was illuminated at 500 MHz where a 4.3 cm diameter bone/fat object was placed approximately 6 cm to the left of the center and a second 5 cm diameter 0.9% saline heated zone was located 4 cm to the right of center. These targets were immersed in a saline tank filled with 0.6% saline. The thermal phantom was heated from 25°C to 45°C.

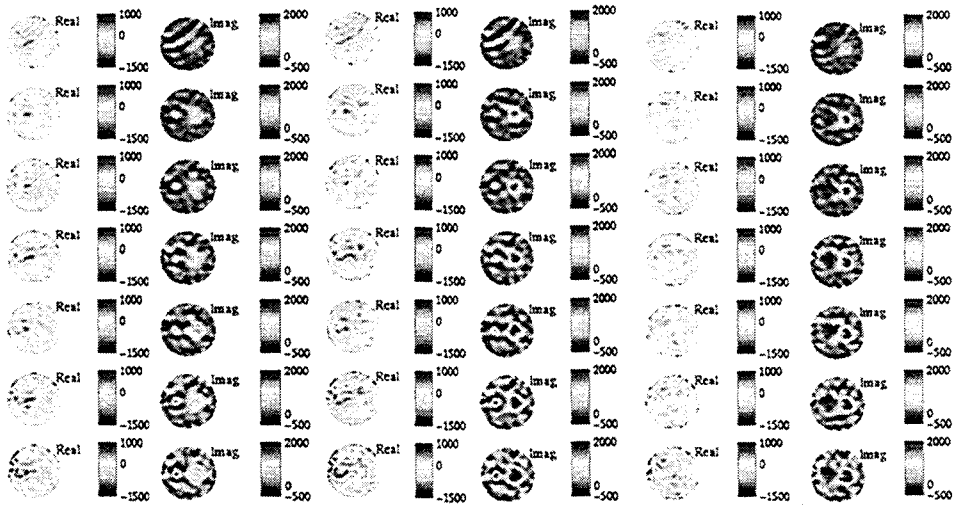

Figure 23: Real (left) and Imaginary (right) component difference of the reconstructed images between the heated and the baseline frames for localized heated and nonheated zones with and without the use of *a priori* information.

The results in Figure 23 are differences between the heated target and the baseline images for both the real and imaginary components of the electrical property distribution. Nonheated regions should have zero difference while heated regions should have blue shading in the real and red shading in the imaginary property components corresponding to the negative and positive temperature coefficients of these quantities. The first image set contains no apriori information. The real component images possess some increasingly red-colored regions which is artifact. The imaginary component images qualitatively reconstruct the effect of heating; however, the quantitative accuracy of the thermal reconstruction is poor. This is confirmed in Figure 24 where the reconstructed values are poorly-fitted to the expected temperature behavior.

The second image set contains apriori data on the heated target location and its dielectric properties can be approximated. There is considerable improvement both in terms of qualitatively interpreting the images as well as quantitatively evaluating them.

Specifically, the heated target zone is much better defined in the imaginary image component, although the images still suggest some heating of the bone/fat object which does not occur physically. The final image set shows further improvements in the reconstructions by providing additional apriori information regarding the location and the approximate dielectric properties of the bone/fat object as well. Now, the bone/fat target does not appear to undergo a temperature rise, in fact, it remains visible in the image because the background saline temperature is shown to elevate slightly. Temperature measurements in the saline confirm that this is the case due to thermal conduction from the heated zone over time. The quantitative temperature estimates for both examples where apriori information is supplied show the significant improvement in the peak value and zone-averaged electrical properties of the heated region as a function of temperature.

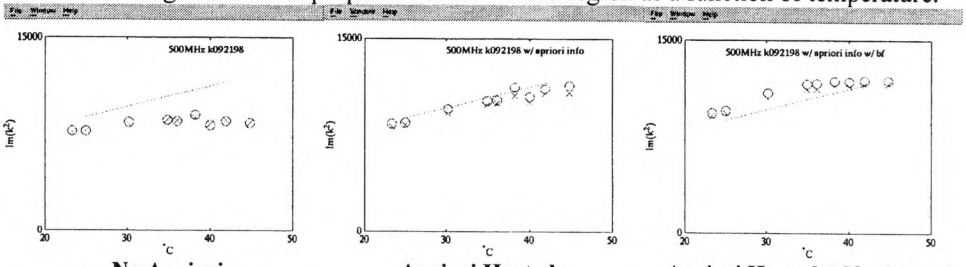

Figure 24: Thermal accuracy of reconstructed images with and without a priori information. Solid line is expected temperature behavior. Open circles are reconstructed temperature value sampled at the center of the heated region. X's are the average reconstructed temperature value sampled over half the area of the heated region.

A number of thermal imaging experiments using an ex-vivo kidney model have also been completed and representative results from this experience are briefly described here. The temperature distributions that develop in this model are complex and require further investigation. An excised fixed porcine kidney has been used in these preliminary thermal evaluations. The kidney was perfused with an externally heated 0.9% saline solution. Temperature and fluid flow rate were controlled by an external circulator. Figure 25 shows a 900 MHz difference image of the imaginary component property distribution for the kidney perfused at 20°C and 25°C. The kidney was 12 cm in length and approximately 4 cm thick, being positioned lengthwise within the imaging plane.

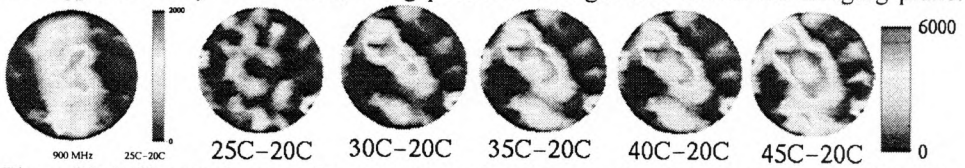

Figure 25: Difference images of an ex-vivo porcine kidney perfused with heated saline: 900 MHz difference image (1st image on left) for kidney perfused at 25°C and 20°C. Series of 700 MHz difference images (2nd through 6th images) over time for increasing temperature of the perfusate.

The outline of the kidney is clearly distinct. Further, the bright central region indicating temperature elevation is where the renal artery was located. Also presented in Figure 25 is a series of 700 MHz difference images of the imaginary component property distribution for the kidney perfused over much longer time periods at higher temperatures of the perfusate. There is a clear progression in the spatial distribution of temperature rise. These results are encouraging from the perspective of imaging a complicated organ structure which produces a complex thermal distribution that evolves over time.

7.4 In Vivo Imaging

As a final example, a series of preliminary in vivo images are shown where a human hand/arm has been raised and lowered within the imaging array. Figure 26 shows reconstructed images and accompanying photographs of different hand positions illuminated at 300 MHz. The top image on the left corresponds to the case where the fingers remain in contact with each other while the thumb is separated by a glass beaker as illustrated in the photograph. The finger group and the isolated thumb are evident in the reconstructed images. In the bottom image, the hand is cupped, but with the fingers pointed in the upward direction. The fingers and palm, along with the intervening saline solution which occupies the cupped portion of the palm, can be located in the image. The second image series in Figure 26 depicts reconstructions of the hand from another set of in vivo experiments using the 32 channel system to acquire measured data over a 24 cm cross-section at 700 MHz. In this case, the length of the hand is positioned parallel to the imaging plane and is moved into this cross-section from below where the imaging plane transects the wrist (upper left image in the series). The progression of images clearly shows the emergence of the palm and the extension of the fingers (bottom right image in the series). The images in Figure 26 are intriguing because they show identifiable features within the hand, wrist and arm areas as the anatomy is raised and lowered through the antenna plane. Further, these images were obtained without any special processing or calibration of the measured data relative to the procedures which are in place for phantom imaging. In this sense, the results in Figure 24 are quite encouraging. Significant improvements are needed, but these can be expected to occur as more experience is gained with in vivo microwave imaging.

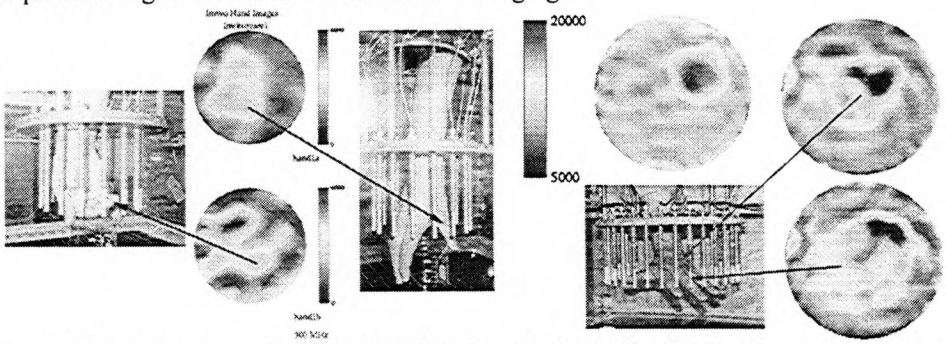

Figure 26: In vivo images of a human hand illuminated at 300 MHz (left) as it is raised and lowered within the 14cm diameter 16 antenna imaging array. Arrows point to the anatomical locations of features found within the imaging planes. 700 MHz set of images (right) obtained in the 26 cm diameter 32 antenna imaging array where the length of the hand is parallel to the imaging plane and is raised into the plane from below.

ACKNOWLEDGMENTS

This work was supported in part by NIH grants R01-CA64588 and R01-CA55034 awarded by the National Cancer Institute.

REFERENCES

1. Duck, F.A., *Physical Properties of Tissue: A Comprehensive Reference Book.* 1990, London: Academic Press.

2. R. Pethig, "Dielectric properties of biological materials: biophysical and medical applications" *IEEE Transactions on Electrical Insulation*, . **EI-19**: p. 453-474 1984.
3. R. Pethig, "Dielectric properties of biological tissues" *Clinical Physics and Physiological Measurements*, . **8**: p. 5-12 1987.
4. S. Mizushina, "Non-invasive temperature measurements. Aspects of medical technology", Gordon and Breach, New York, 1987.
5. F. Bardati, V.J. Brown and P. Tognolatti, "Temperature reconstructions in a dielectric cylinder by multifrequency microwave radiometry", *J. Electromagn Wave Appl,* **7**, 1993.
6. S. Mizushina, T. Shimizu and T. Sugiura, "Non-invasive thermometry with multi-frequency microwave bradiometry, *Front Med Biol Eng.*, **4**, 129-133.
7. L. Dubois, J. Pribetich, J.J. Fabre, M. Chive and Moschetto, "Non-invasive microwave multifrequency radiometry used in microwave hyperthermia for bidimensional reconstruction of temperature patterns", *Int. J. Hyperthermia*, **9**(3), 415-431.
8. J.F. Head and R.L. Elliot, "Thermography: its relation to pathologic characteristics, vascularity, proliferation rate, and survival of patients with invasive ductal carcinoma of the breast", *Cancer*, **79**, 186-187, 1997.
9. J.R. Keyserlingk, P.D. Ahlgren, E. Yu and N. Belliveau, "Infrared Imaging of the breast: initial reappraisal using high-resolution digital technology in 100 successive cases of stage I and II breast cancer", *The Breast Journal*, **4**(4), 245-251, 1998.
10. M. Plancot, B. Prevost, M. Chive, J.J. Fabre, L. Ledel and G. Giaux, "A new method for thermal dosimetry in microwave hyperthermia using microwave radiometry for temperature control", *Int J. Hyperthermia*, **3**(1), 9-19.
11. M. Chive, "Use of microwave radiometry for hyperthermia monitoring and as a basis for thermal dosimetry", M. Gautherie (ed), 113-128, Springer Berlin Heidelberg New York, 1990.
12. C. Gabriel, S.Gabriel and E. Corthout, "The dielectric properties of biological tissues: I. literature survey" *Phys. Med. Biol.*, . **41**: p. 2231-2249 1996.
13. S. Gabriel, R.W. Lau and C. Gabriel, "The dielectric properties of biological tissues: II. measurements in the frequency range 10 Hz to 20 GHz" *Phys. Med. Biol.*, . **41**: p. 2251-2269 1996.
14. S. Gabriel, R.W. Lau and C. Gabriel, "The dielectric properties of biological properties: III. parametric models for the dielectric spectrum of tissues" *Phys. Med. Biol.*, . **41**(2271-2293) 1996.
15. D.C. Brown and B.H. Brown, "Imaging spatial distribution of resistivity using applied potential tomography" *Electronics Lett.*, . **19**(22): p. 933-935 1983.
16. M. Vogelius and F. Santosa, "A backprojection algorithm for electrical impedance imaging" *SIAM J. Appl. Math.*, . **50**: p. 216-243 1990.
17. R. Guardo, C. Bourlay, B. Murray and M. Bertrand, "An experimental study in electrical impedance tomography using backprojection reconstruction" *IEEE Trans Biomed. Eng.*, . **38**: p. 617-627 1991.
18. D.C. Barber, and N.J. Avis "Image reconstruction using non-adjacent drive configurations" *Physiol. Meas.*, . **15**(Suppl. A): p. A153-A160 1994.
19. B.H. Brown, D.C. Brown, W. Wang, L. Lu, A.D. Leathard, R.H. Smallwood, A.R. Hampshire, R. Mackay and K. Hatzigalanix, "Multi-frequency imaging and modeling of repiratory related electrical impedance changes" *Physiol. Meas.*, . **15**(Suppl. 2A): p. A1-A11 1994.

20. A. Adler, R. Amyot, R. Guardo, J.H.T. Bates and Y. Berthiaume, "Monitoring changes in lung air and liquid volumes with electrical impedance tomography" *J. Appl. Physiol.*, . **83**: p. 1762-1767 1997.
21. J.Y. Yorkey, J.G. Webster and W.J. Tompkins, "Comparing reconstruction algorithms for electrical impedance tomography" *IEEE Trans. Biomed. Eng.*, . **BME-34**(11): p. 843-852 1987.
22. J.G. Webster and J.G. Hua, "A regularised electrical impedance tomography reconstruction algorithm" *Clin. Phys. Physiol. Meas.*, . **9**(Suppl. A): p. 137-141 1988.
23. M. Cheney, D.Isaacson, J.C. Newell, S. Simske and J. Goble, "NOSER: an algorithm for solving the inverse conductivity problem" *International Journal of Imaging Systems and Technology*, . **2**: p. 66-75 1991.
24. K.D. Paulsen, M.J. Moskowtiz and T.P. Ryan, "Temperature field estimation using electrical impedance profiling methods: I. reconstruction algorithm and simulated results" *Int. J. Hyperthermia*, . **10**: p. 209-228 1994.
25. A.D. Seagar, D.C. Barber and B.H. Brown, "Electrical impedance imaging" *IEE Proceedings*, . **134**: p. 201-210 1987.
26. D.C. Brown and B.H. Brown, "Applied potential tomography" *J. Phys. E:Sci. Instrum.*, . **17**: p. 723-732 1984.
27. D.C. Barber, B.H. Brown and .I.L. Freeston, "Imaging spatial distributions of resistivity using applied potential tomography" *Electronic Lett.*, . **19**(22): p. 933-935 1983.
28. A.D. Seagar and B.H. Brown, "The Sheffield data collection system" *Clin. Phys. Physiol. Meas.*, . **8**(Suppl. A): p. 91-97 1987.
29. A.D. Seagar and D.C. Brown, "Fast reconstruction of resistance images" *Clin. Phys. Physiol Meas.*, . **8**(Suppl. A): p. 47-54 1987.
30. D.H. Brown and D.C. Barber, "Errors in reconstruction of resistivity images using a linear reconstruction technique" *Clin. Phys. Physiol. Meas.*, . **9**(Suppl. A): p. 101-104 1988.
31. D.H. Brown and D.C. Barber, "Possibilities and prblems of realtime imaging of tissue resistivity" *Clin. Phys. Physiol Meas.*, . **9**(Suppl. A.): p. 121-125 1988.
32. D.C. Barber, "A sensitivity method for electrical impedance tomography" *Clin. Phys. Physiol. Meas.*, . **10**: p. 368-371 1989.
33. D.H. Brown and D.C. Barber, "Progress in electrical impedance tomography, inversed problems in partial differential equations" *SIAM*, : p. 151-154 1990.
34. B.H. Brown, A.D. Leathard, L. Lu, W. Wang and A. Hampshire, "Measured and expected Cole parameters from electrical impedance tomographic spectroscopy images of the human thorax" *Physiol. Meas.*, . **16**(Suppl. 3A): p. A57-A67 1995.
35. B.H. Brown, D.C. Barber, A.D. Leathard, L. Lu, W. Wang, R.H. Smallwood and A.J. Wilson, "High frequency EIT data collection and parametric imaging" *Innov. Tech. Biol. Med.*, . **15**(No. Special 1): p. 1-8 1994.
36. B.H. Brown, D.C. Barber, W. Wang, L. Lu, A.D. Leathard, R.H. Smallwood, A.R., Hampshire, R. Mackay and K. Hatzigalanis, "Multi-frequency imaging and modelling of respiratory related lectrical impedance changes" *Physiol. Meas.*, . **15**(Suppl. 2A): p. A1-A11 1994.
37. J.C. Newell, D. Isaacson and D.G. Gisser, "An electric current tomograph" *IEEE Trans Biomed Eng.*, . **35**(10): p. 823-833 1988.
38. J.C. Newell, P.M. Edic, X. Ren, J.L. Larson-Wiseman and M.D. Danyleiko, "Assessment of acute pulmonary edema in dogs by electrical impedance imaging" *IEEE Trans. Biomed. Eng.*, . **43**: p. 133-138 1996.

39. R.D. Cook, G.J. Soulnier, D.G. Gisser, J.C. Goble, J.C. Newell and D. Isaacson, "ACT3: A high-speed, high precision electrical impedance tomograph" *IEEE Transactions on Biomedical Engineering*, . **41**: p. 713-722 1994.
40. P.M Edic, G.J. Sounier, J.C. Newell and D. Isaacson, "A real-time electrical impedance tomograph" *IEEE Trans. Biomed. Eng.*, . **42**: p. 849-859 1995.
41. D. Isaacson, "Distinguishability of conductivities by electric current computed tomography" *IEEE Trans. Biomed. Eng.*, . **MI-5**(2): p. 91-95 1986.
42. M. Cheney, D.I.a.E.I.I., "Exact solutions to a linearised inverse boundary value problem" *Inverse Problems*, . **6**: p. 923-934 1990.
43. M. Cheney, D. Isaacson and E.L. Isaacson, "Current problems in impedance imaging, Inverse problems in partial differential equations" *SIAM*, : p. 141-149 1990.
44. D. Isaacson and M. Cheney, "An overview of inversion algorithms for impedance imaging" *Contemp. Math.*, . **122**: p. 29-39 1990.
45. K.S. Cheng, D. Isaacson, J.C. Newell and D.G. Gisser, "Electrode model for electric current computed tomography" *IEEE Trans Biomed. Eng.*, . **36**: p. 918-924 1989.
46. J. Conway, "Electrical impedance tomography for thermal monitoring of hyperthermic treatment: an assessment using in vitro and in vivo measurements" *Clinical Physics and Physiological Measurements*, . **8**: p. 141-146 1987.
47. S. Ahmed and S. Griffiths, "Applied potential tomography for non-invasive temperature mapping in hyperthermia" *Clinical Physics and Physiological Measurements*, . **8**: p. 147-153 1987.
48. M.S. Hawley, J. Conway, H. Amasha, Y.F. Mangnall and G.C. Van Rhoon, "Electrical impedance tomography: prospects for non-invasive control of deep hyperthermia treatments" *Frontiers in Medical and Biological Engineering*, . **4**: p. 119-128 1992.
49. B. Blad, B. Persson and K. Lindstrom, "Quantitative assessment of impedance tomography for temperature measurements in hyperthermia" *International Journal of Hyperthermia*, . **8**: p. 33-43 1992.
50. M.J. Moskowitz, K.D. Paulsen and T.P. Ryan, "Temperature field estimation using electrical impedance profiling methods: II experimental system description and phantom results" *Int. J. Hyperthermia*, . **10**: p. 229-245 1994.
51. K.D. Paulsen, M.J. Moskowitz, T.P. Ryan and S.E. Mitchell, "Initial in vivo experience with EIT as a thermal estimator during hyperthermia" *Int. J. Hyperthermia*, . **12**: p. 573-591 1996.
52 M.J. Moskowitz, T.P. Ryan, K.D. Paulsen and S.E. Mitchell, "Clinical implementation of electrical impedance tomography with hyperthermia" *International Journal of Hyperthermia*, . **11**: p. 141-149 1995.
53. H. Jaing and K.D. Paulsen, "An Enhanced Electrical Impedance Imaging Algorithm for Hyperthermia Applications" *International Journal of Hyperthermia*, . **13**: p. 459-480 1997.
54. M.A. Esrick and D.A. McRae, "Deconvolved electrical impedance spectra track distinct cell morphology changes" *IEEE Trans. Biomed. Eng.*, . **43**: p. 607-618 1996.
55. C.S. Koukourlis, G.A. Kyriacou and J.N. Sahalos, "A 32-electrode data collection system for electrical impedance tomography" *IEEE Transactions on Biomedical Engineering*, . **42**: p. 632-636 1995.
56. R.W.M. Smith, I.L. Freeston and B.H. Brown, "A real-time electrical impedance tomography system for clinical use-design and preliminary results" *IEEE Transactions on Biomedical Engineering*, . **42**: p. 133-140 1995.

57. A. Hartov, R. Mazzarese, F. Reiss, T. Kerner, S. Osterman, D. Williams and K. Paulsen, "A multi-channel continuously-selectable multi-frequency electrical impedance spectroscopy measurement system", *IEEE Transactions on Biomedical Engineering*, (In press), 1998.
58. T. Kerner, D. Williams, K. Osterman, F. Reiss, A. Hartov, K. Paulsen, *Electrical Impedance Imaging at Multiple Frequencies in Phantoms*, University College London, England, 1999.
59. J.C. Bolomey, J. Izadnegahdar, L. Jofre, C.H. Pichot, G. Peronnet and M. Solaimani, "Microwave diffraction tomography for biomedical applications" *IEEE Trans. Microwave Theory Tech.*, . **30**: p. 1990-2000 1982.
60. J.C. Bolomey, "Recent European developments in active mircrowave imaging for industrial, scientific and medical applications" *IEEE Trans. Microwave Theory Tech.*, . **37**: p. 2109-2117 1989.
61. J.H. Jacobi and L. E. Larsen, *Medical applications of microwave imaging*. 1986. New York: IEEE.
62. J.C. Lin, "Frequency optimization for microwave imaging of biological tissues" *Proc. IEEE*, . **73**: p. 374-375 1985.
63. R. Maini, M.F. Iskander, C.H. Durney and M. Berggren, "On the sensitivity and resolution of microwave imaging using ART" *Proc. IEEE*, . **69**: p. 1517-1519 1981.
64. R. Maini, M.F. Iskander and C.H. Durney, "On electromagnetic imaging using linear reconstruction techniques" *Proc IEEE*, . **68**: p. 1550-1552 1980.
65. J.C. Bolomey, C. Pichot and Gaboriavd, "Planar microwave imaging camera for biomedical applications: critical and prospective analysis of reconstruction algorithms" *Radio Science*, . **26**: p. 541-550 1991.
66. L. Jofre, M.S. Hawley, A. Broquetas E. de los Reyes, M. Ferrando and A.R. Elias-Fuste, "Medical imaging with a miecrowave tomographic scanner" *IEEE Trans. Biomed. Eng.*, . **37**: p. 303-312 1990.
67. A. Broquetas, J. Romeu, J.M. Rius, A.R. Elias-Fuste, A. Cardama and L. Jofre, "Cylindrical geometry: a further step in active microwave tomography" *IEEE Trans. Microwave Theory Tech.*, **39**: p. 836-844 1991.
68. M. Miyakawa, "Tomographic measurement of temperature change in phantoms of the human body by chirp rada-type microwave computed tomography" *Med. Biol. Eng. Comput.*, . **31**: p. S31-S36 1993.
69. J.C. Bolomey, L. Jofre and G. Peronnet, "On the possible use of microwave-active imaging for remote thermal sensing" *IEEE Trans. Microwave Theory Tech.*, . **31**: p. 777-781 1983.
70. S. Caorsi, G.L. Gragnani and M. Pastorino, "A multi-view microwave imaging system for two dimensional penetrable objects" *IEEE Trans. Microwave Theory Tech.*, . **39**: p. 845-851 1991.
71. S. Caorsi, G.L. Gragnani and M. Pastorino, "Reconstruction of dielectric permittivity distributions in arbitrary 2D inhomogeneous biological bodies by a multiview microwave numerical method" *IEEE Trans. Med. Imaging*, . **12**: p. 632-640 1993.
72. S. Caorsi, S. Ciaramella, G.L. Gragnani and M. Pastorino, "On the use of regularization techniques in numerical inverse scattering solutions for microwave imaging applications" *IEEE Trans. Microwave Theory Tech.*, . **43**: p. 632-640 1995.
73. N. Jaochimowicz, C. Pichot and R. Hugonin, "Inverse scattering: an iterative numerical method for electromagnetic imaging" *IEEE Trans Antennas Propagat.*, . **39**: p. 1742-1752 1991.

74. J.M. Rius, C. Pichot, L. Jofre, J.C. Bolomey, N. Joachimowicz, A. Broquetas and M. Ferrando, "Planar and cylindrical active microwave temperature imaging: numerical simulations" *IEEE trans. Med. Imaging*, . **11**: p. 457-469 1992.
75. N. Joachimowicz, J.J. Mallorqui, J.C. Bolomey and A. Broquetas, "Convergence and staqbility assessment of Newton-Kantorovich reconstruction algorithms for microwave tomography" *IEEE Trans. Med. Imaging*, . **17**(4): p. 562-570 1998.
76. S.Y. Semenov, A.E. Bulyshev, A.E. Souvorov, R.H. Svenson, Y.E. Sizov, V.Y. Borisov, V.G. Posukh, I.M. Kozlov, A.G. Nazarov and G.P. Tatsis, "Microwave tomography: theoretical and experimental investigation of the iteration reconstruction algorithm" *IEEE Trans. Microwave Theory Tech.*, . **46**(2): p. 133-141 1998.
77. C. Pichot and A. Franchois, "Microwave imaging-complex permittivity reconstruction with a Levenberg-Marquardt method" *IEEE Trans. Antennas Propagat.*, . **45**: p. 230-215 1997.
78. P.M. Meaney, K.D. Paulsen and T.P. Ryan, "Two-dimensional hybrid element image reconstruction for TM illumination" *IEEE Trans. Antenn. Propagat.*, . **43**: p. 239-247 1995.
79. S. Caorsi, G.L. Gragnani, S. Medicina, M. Pastorino and G. Zunino, "Microwave imaging based on a Markov random field model" *IEEE Trans. Antennas Propagat.*, . **42**: p. 293-303 1994.
80. S. Caorsi, G.L. Gragnani, S. Medicina, M. Pastorino and G.A. Pinto, "A Gibbs random field-based active electromagnetic method for noninvasive diagnostics in biomedical applications" *Radio Sci.*, . **30**: p. 291-301 1995.
81. S. Caorsi, G.L. Gragnani, S. Medicina, M. Pastorino and G. Zunino, "Microswave imaging using a simulated annealing approach" *IEEE Microwave Guided Wave Lett.*, : p. 331-333 1992.
82. J.H. Jacobi and L.E. Larsen, "Methods of active microwave imagery for dosimetric applications" *Medical Applications of Microwave Imaging*, : p. 118-137 1986.
83. J.J. Mallorqui, A. Broquetas, L. Jofre and A. Cardama, "Non-invasive active thermometry with a microwave tomographic scanner in hyperthermia treatments" *Applied computational electromagetics Society Journal*, . **7**(2): p. 121-127 1992.
84. M.S. Hawley and J. C. Bolomey, *Non-invasive control of hyperthermia.* in *Clinical Thermology Subseries Thermotherapy.* 1989. Springer, Berlin.
85. M. Miyakawa, "Tomographic imaging of temperature change in a phantom of human body using of chirp radar-type imcrowave tomograph" *Med. & Biol. Eng. Comput.*, . **29**(2): p. 745 1991.
86. M. Miyakawa, D. Watanabe, T. Hayashi and Y. Saitoh, "Tomographic measurement of temperature change in phantoms of the human body by chirp rada-type microwave computed tomography" *Med. Biol. Eng. Comput.*, . **31**: p. S31-S36 1993.
87. P.M. Meaney, K.D. Paulsen, A. Hartov and R.K. Crane, "An active microwave imaging system for reconstruction of 2D electrical property distributions" *IEEE Trans. Biomed. Eng.*, . **42**: p. 1017-1026 1995.
88. P.M. Meaney, K.D. Paulsen, A. Hartov and R.K. Crane, "Multi-target microwave imaging for tissue assessment: inital evaluation in tissue-equivalent phantoms" *IEEE Trans. Biomed. Engr.*, . **43**: p. 878-890 1996.
89. P.M. Meaney, K.D. Paulsen and .J. Chang, "Near-field microwave imaging of biologically-based materials using a monopole system" *IEEE Microwave Theory Tech.*, . **46**: p. 31-45 1998.

90. P.M. Meaney, K.D. Paulsen, J.T. Chang and M. Fanning. *Towards a Clinical Implementation of a Non-Invasive Microwave Imaging System for Temperature Monitoring.* in *Proceedings SPIE BIOS 98 International Symposium*. 1998.
91. P.M. Meaney, K.D. Paulsen, J.T. Chang, M. Fanning and A. Hartov, "Nonactive antenna compensation for fixed array microwave imaging: Part II imaging results" *IEEE Trans Medical Imaging*, . **18**: p. 508-518 1999.
92. J.T. Chang, K. Paulsen, P. Meaney and M. Fanning, "Non-invasive thermal assessment of tissue phantoms using an active near field microwave imaging technique" *Int. J. Hyperthermia*, . **14**(6): p. 513-534 1998.
93. A. Franchois, A. Joisel, C. Pichot and J.C. Bolomey, "Quantitative microwave imaging with a 2.45-GHz planar microwave camera", *IEEE Trans. Med. Imag.*, **17** 550-561, 1998.
94. S.Y. Semenov, R.H. Svenson, A.E. Boulyshev, A.E. Souvorov, V.Y. Borisov, Y. Sizov, A.N. Starostin, K.R. Dezern, G.P. Tasis and V.Y. Baranov, "Microwave Tomography: Two-Dimensional System for Biological Imaging", *IEEE Trans. Bio. Eng.*, **43**(9), 869-877, 1996.
95. K.D. Paulsen and P.M. Meaney, "Nonactive Antenna Compensation for Fixed-Array Microwave Imaging—Part I: Model Development", *IEEE Trans. Medical Imaging*, **18**(6), 496-507, 1999.